Spallation residues in the reaction ^{56}Fe+ p at 0.3A, 0.5A, 0.75A, 1.0A, and 1.5A GeV

C. Villagrasa-Canton,[1,*] A. Boudard,[1,†] J.-E. Ducret,[1] B. Fernandez,[1] S. Leray,[1] C. Volant,[1] P. Armbruster,[2] T. Enqvist,[2] F. Hammache,[2] K. Helariutta,[2] B. Jurado,[2] M.-V. Ricciardi,[2] K.-H. Schmidt,[2] K. Sümmerer,[2] F. Vivès,[2] O. Yordanov,[2] L. Audouin,[3] C.-O. Bacri,[3] L. Ferrant,[3] P. Napolitani,[2,3,‡] F. Rejmund,[3,§] C. Stéphan,[3] L. Tassan-Got,[3] J. Benlliure,[4] E. Casarejos,[4] M. Fernandez-Ordoñez,[4,‖] J. Pereira,[4,¶] S. Czajkowski,[5] D. Karamanis,[5] M. Pravikoff,[5] J. S. George,[6] R. A. Mewaldt,[6] N. Yanasak,[6] M. Wiedenbeck,[7] J. J. Connell,[8] T. Faestermann,[9] A. Heinz,[10] and A. Junghans[11]

[1]*DAPNIA/SPhN, CEA/Saclay, F-91191 Gif-sur-Yvette Cedex, France*

[2]*GSI, Planckstrasse 1, D-64291 Darmstadt, Germany*

[3]*IPN Orsay, BP 1, F-91406 Orsay Cedex, France*

[4]*University of Santiago de Compostela, 15706 Santiago de Compostela, Spain*

[5]*CEN Bordeaux-Gradignan, UMR 5797 CNRS/IN2P3-Université Bordeaux 1, BP 120, F-33175 Gradignan, France*

[6]*California Institute of Technology, Pasadena, California 91125, USA*

[7]*Jet Propulsion Laboratory, California Institute of Technology, Pasadena, California 91109, USA*

[8]*University of New Hampshire, Durham, New Hampshire 03824, USA*

[9]*TU Munich, D-85747 Garching, Germany*

[10]*Argonne National Laboratory, Argonne, Illinois 60439-4083, USA*

[11]*Institüt für Strahlenphysik, Postfach 510119, D-01314 Dresden, Germany*

(Received 24 October 2006; published 13 April 2007)

The spallation residues produced in the bombardment of ^{56}Fe at 1.5A, 1.0A, 0.75A, 0.5A, and 0.3A GeV on a liquid-hydrogen target have been measured using the reverse kinematics technique and the fragment separator at GSI (Darmstadt). This technique has permitted the full identification in charge and mass of all isotopes produced with cross sections larger than 10^{-2} mb down to $Z = 8$. Their individual production cross sections and recoil velocities at the five energies are presented. Production cross sections are compared with previously existing data and with empirical parametric formulas, often used in cosmic-ray astrophysics. The experimental data are also extensively compared with the results of different combinations of intranuclear cascade and deexcitation models. It is shown that the yields of the lightest isotopes cannot be accounted for by standard evaporation models. The GEMINI model, which includes an asymmetric fission decay mode, gives an overall good agreement with the data. These experimental data can be directly used for the estimation of composition modifications and damages in materials containing iron in spallation sources. They are also useful for improving high-precision cosmic-ray measurements.

DOI: 10.1103/PhysRevC.75.044603 PACS number(s): 25.40.Sc, 25.70.Mn, 21.60.Ka

I. INTRODUCTION

The spallation cross sections of nuclides such as Fe have been historically studied to understand the propagation of cosmic-ray ions in the galaxy and to determine the composition of the galactic cosmic ray (GCR) source [1–9]. Galactic cosmic rays constitute a superthermal gas that is partially confined in the galaxy by interstellar magnetic fields with some leakage into the intergalactic medium. While propagating in the galaxy, cosmic rays pass through the interstellar medium, and some primary cosmic-ray nuclei spallate into secondary cosmic-ray nuclei. As measured by instruments in the solar system, the composition includes both primary cosmic rays whose abundance is depleted by spallation, and secondary cosmic rays produced by spallation. As a result of spallation during propagation, certain elements are far more abundant (often by orders of magnitude) in the GCRs than in solar system material. Examples of these "secondary elements" include Li, Be, and B (which are mainly spallation products of C and O) and Sc, Ti, V, and Cr (which are mainly spallation products of Fe). Conversely, those elements for which the contribution from heavier elements is much smaller and hence have very small secondary contributions are "primary elements." Prominent examples include C, O, and Fe. Provided the spallation cross sections are known, the abundance of secondary elements relative to primary elements are a measure of the amount of material cosmic rays traverse in the galaxy. This in turn constrains astrophysical models of cosmic rays in the galaxy. It is possible to correct abundance measurements for propagation back to the "source," that is, to determine the composition of the material that became the cosmic rays. The secondary-to-primary ratios combined with the cross sections determine the amount of material traversed during propagation in the galaxy; the amount of material traversed, again with the cross sections, is then used to correct the measured abundances to the source abundances. Thus, uncertainties in the cross sections

*Present address: IRSN, BP 17, F-92262 Fontenay-aux-Roses Cedex, France.

†Electronic address: Alain.Boudard@cea.fr

‡Present address: LPC-Caen, F-14050 Caen Cedex , France.

§Present address: GANIL, BP 55027, F-14076 Caen Cedex 05, France.

‖Present address: CIEMAT, Avda. Complutense, 22, E-28040 Madrid, Spain.

¶Present address: NSCL, E. Lansing, MI 48824, USA.

are more significant than any details of the astrophysical models. (The exceptions to this generalization are the unstable secondaries.) In recent years, new high-resolution elemental and isotopic measurements have become available (i.e., the ACE [10] and Ulysses [11] space missions), including measurements in the iron region. The main source of uncertainties in determining both cosmic-ray secondary production and source composition using these data are uncertainties in the nuclear cross sections. The interstellar medium is composed ∼90% by the number of H atoms and ions. Most high-resolution measurements are of cosmic rays with energies per nucleon in the interstellar medium of ∼0.5–1.5 GeV. The cross sections reported here are thus directly applicable to the improved interpretation of high-precision cosmic-ray measurements.

Spallation reactions have also gained a renewed interest with the recent projects of spallation neutron sources and accelerator-driven subcritical reactor systems considered for the transmutation of nuclear waste [accelerator-driven systems (ADS)]. In these systems, a high-intensity proton beam of energy around 1 GeV is guided on a spallation target made of a high-mass material. In ADS, neutrons produced in the spallation target are used to maintain the reactivity in the subcritical reactor where nuclear waste can be transmuted. The proton beam under vacuum in the accelerator has generally to cross a window before entering the spallation target. As it is continuously submitted to the proton beam irradiation, it is one of the most sensitive parts in ADS or spallation-neutron-source design. Among the problems created by the proton irradiation are changes in the chemical composition of the window material and embrittlement created by gas production and atomic displacements (DPA) in the crystal lattice. A large range of materials have been studied for this window and, in most of the projects, martensitic steels composed of 90% iron (with also substantial quantities of chromium and molybdenum) have been retained due to their resistance to thermal constraints and radiation effects. Therefore, it is important to have a good knowledge of the production cross sections of spallation residues in iron and of their recoil velocity.

In recent years, an important effort has been undertaken, mainly under the framework of the HINDAS European project [12], to collect a comprehensive set of high-quality spallation data regarding the production of neutrons [13,14], light charged particles [15], and residual nuclei. The general goal is to better understand the reaction mechanisms in order to improve the models implemented into high-energy transport codes. These codes, validated on experimental data, can afterward be used to reliably predict all quantities needed for the design of ADS or spallation sources as neutron production, activation, or damages.

As concerns residue production, up to now the emphasis has been on spallation reactions on heavy nuclei. Isotopic cross sections of residues produced in the reactions ^{197}Au + p [16,17] at 800A MeV, ^{208}Pb + p at 1A GeV and 500A MeV [18–21], ^{238}U + p at 1A GeV [22,23], and ^{238}U + d at 1A GeV [24,25] have already been measured using the reverse-kinematics method at GSI (Darmstadt). In this paper, we present new experimental results concerning the isotopic production cross sections and recoil velocities of spallation residues in the reaction ^{56}Fe+ p for five energies of the iron beam: (0.3, 0.5, 0.75, 1.0, and1.5)A GeV. This measurement is the first consistent set of data on isotopically identified residues on a large energy domain and for a light nucleus of practical interest. The comparison of the obtained data with various models, some of them being quite successful for heavy systems, allows testing of their predicting capabilities for light nuclei and their dependence on beam energy.

II. EXPERIMENTAL METHOD

A. Experimental setup

In October 2000, an experiment was performed using the reverse kinematics at GSI in Darmstadt, Germany. A primary beam of ^{56}Fe was delivered by the heavy-ion synchrotron Schwerionen Synchrotron (SIS) at energies of (0.3, 0.5, 0.75, 1.0 and 1.5)A GeV and directed onto a liquid-hydrogen target designed and built in the Laboratoire National Saturne (Saclay, France) [26].

The liquid-hydrogen thickness was 87.3 mg/cm^2 contained by titanium windows of 20 μm each. Two additional Ti foils were used to isolate the vacuum around the target from the vacuum of the beam pipe for security reasons so that a total of 36 mg/cm^2 of Ti contributed to the empty-target counting. Measurements were repeated with an identical empty target in order to subtract the production on the titanium container from the measured yields of residual nuclei. The contribution of these walls to the counting rates was below 10% for the main part of the residues and below 20% for the lightest ones.

The time structure of the primary beam was a pulse of 6 s every 12 s, and the intensity was limited to 10^7 ions/spill. This beam intensity was measured using a secondary-electron emission monitor (SEETRAM) [27] calibrated at the beginning and at the end of each set of measurements at a given beam energy. This was done at low counting rates with a plastic scintillator as absolute reference.

Residual nuclei produced in the reaction with the target were focused in the beam direction and analyzed with the FRS (fragment separator) [28] operated as an achromatic magnetic spectrometer. Figure 1 is a schematic diagram of the experimental setup showing the four large dipole magnets and the essential detector equipment.

Due to their relativistic energies, the fragments produced in this experiment are fully stripped. The horizontal positions of these ions and the time of flight (TOF) were measured with two plastic scintillators, one located in the intermediate dispersive plane S2 and the other one installed at the final achromatic focal plane S4. The signal from the scintillator at S4 was used as the trigger for the acquisition of all detectors. The nuclear charge Z was determined using a multiple-sampling ionization chamber (MUSIC). The energy loss in the gas produces a signal proportional to Z^2/β^2, allowing the determination of Z with a resolution of $\Delta Z = 0.3$ (full width at half maximum) charge units.

The knowledge of the horizontal positions of the ions determines precisely the radii $\rho 1$ and $\rho 2$ of their trajectories in the two magnetic sections of the spectrometer. An absolute

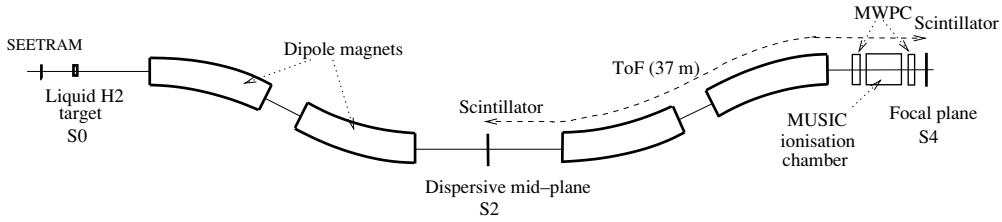

FIG. 1. Schematic layout of fragment spectrometer. Fragments are analyzed by the four large dipole magnets. Scintillators at S2 and S4 measure the time of flight over the second half of the spectrometer as well as the horizontal positions in the dispersive focal planes at S2 and at S4. The MUSIC detector (ionization chamber) gives information about the energy loss of the fragment. Multiwire proportional chambers (MWPCs) are used for beam tuning and removed for production measurements.

calibration is obtained with the iron beam detected in specific measurements at low intensity. Together with the magnetic field strengths in the dipoles measured with Hall-effect probes, the magnetic rigidities $B\rho 1$ and $B\rho 2$ can be determined for each ion. Therefore, a total identification of the nature of the ions could be performed from the relation

$$\frac{A}{Z} = \frac{eB\rho}{m_u c\beta\gamma}, \tag{1}$$

where m_u was the atomic mass unit and $\beta\gamma$ were deduced from the experimental time of flight. Note that in this formula, we have replaced the mass of the (A, Z) ion by Am_u, which means binding energies are neglected when compared to nucleon masses. The FRS has a momentum acceptance of $\pm 1.5\%$. Therefore, about 18–20 different settings of the FRS were needed to cover the complete velocity distribution of all the ions. Figure 2 shows the complete fragment coverage in the Z vs. A/Z plane for 1 GeV per nucleon ^{56}Fe on the hydrogen target. The plot was made by adding histograms from individual settings, each one normalized to the dose of the primary beam. Fragments are well resolved and easily identifiable in this plot down to lithium. However, for the lightest elements, the transmission of the spectrometer is very low, necessitating a dedicated method of analysis. This has been done only at 1 GeV per nucleon and reported in a separate paper [29]. Therefore, we show in this paper

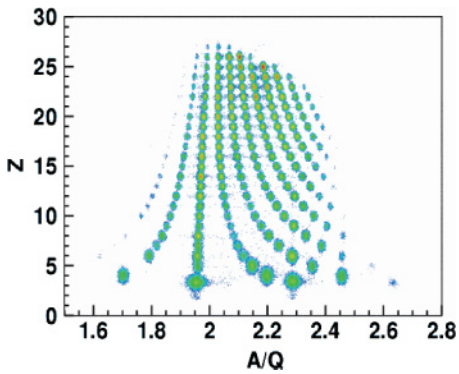

FIG. 2. (Color online) Complete isotope coverage in Z vs. A/Q (actually identical to A/Z) for $1A$ GeV ^{56}Fe on the liquid-hydrogen target. The plot is built from data of overlapping settings, normalized to the primary beam intensity and superimposed.

results of the production cross section and recoil velocity only down to $Z = 8$–10, depending on the beam energy considered.

B. Data analysis

The fragments are first identified in Z using the ionization chamber, taking into account the position and velocity dependence of the energy-loss signal. The velocity distribution of the fragments is obtained with high precision using the time-of-flight and magnetic-rigidity measurements. The experimental TOF between the intermediate and final focal plane is precise enough for an unambiguous identification of the fragment mass. After identification of the isotope, a more accurate value of the longitudinal velocity can be deduced from the magnetic rigidity in the first part of the spectrometer using relation (1).

Assuming that the reaction takes place at the center of the target, the fragment velocity is corrected for the energy loss in the target and transformed into the reference frame of the projectile at rest. A measurement of the recoil velocity of the fragments is thus obtained in that frame. To obtain the production cross section of a given isotope, it is necessary to reconstruct the full velocity distribution by adding the partial ones measured in different settings, with the proper normalization. An example of the velocity distribution for ^{38}K is shown in Fig. 3. For this isotope, five different settings of the FRS were needed to reconstruct the complete velocity distribution.

Due to potential damage to the detectors, isotopes having a magnetic rigidity too close to that of the beam could not be measured. Therefore, the detection of ^{54}Mn was not possible in this experiment. For the same reason, some settings of other isotopes could not be obtained, leading to truncated measured velocity distributions. In that case a fit by a Gaussian function excluding the truncated zones was used to reconstruct the full distribution and then determine the total cross section and the mean value of the velocity and its variance. When a truncated zone in the velocity distribution was too large to have a converging fit, the parameters of the Gaussian were constrained using the neighboring isotopes. The reconstruction procedure leads to an uncertainty on both the velocity determination and the isotope production cross section. These uncertainties have been estimated by taking into account the fluctuation

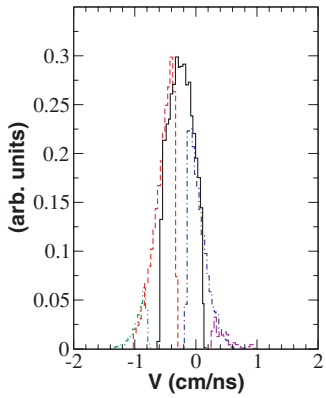

FIG. 3. (Color online) Longitudinal velocity distribution of ^{38}K detected as a residual nucleus at 1A GeV and expressed in the rest frame of the iron beam. Five different settings of the FRS were needed to reconstruct the complete distribution. The yield (here in arbitrary units) detected in each setting is normalized by the number of incident iron nuclei and corrected for the acquisition dead time.

of the reaction point in the target and by doing reasonable variations of the fitted parameters for several groups of isotopes.

C. Corrections and uncertainties

The isotopic production cross section of each spallation residue $\sigma(Z, A)$ was obtained from the difference between the yield measured with the hydrogen target $Y_H(Z, A)$ and the yield measured with the empty target $Y_e(Z, A)$, each of which were corrected for their dead time [correction factor $f_{\tau H}(f_{\tau e})$] and normalized to the number of incident iron nuclei $N_{\mathrm{Fe}H}$ ($N_{\mathrm{Fe}e}$), that is,

$$\sigma(Z, A) = \left(\frac{Y_H(Z, A)\, f_{\tau H}}{N_{\mathrm{Fe}H}} - \frac{Y_e(Z, A)\, f_{\tau e}}{N_{\mathrm{Fe}e}}\right) \times \frac{f_\epsilon\, f_{\mathrm{trans}}\, f_{\mathrm{sec}}}{N_H}. \quad (2)$$

The cross section is finally obtained after a division by the number of hydrogen nuclei per surface unit N_H and with additional corrections due to the detection efficiency f_ϵ, the transmission of the FRS (f_{trans}) and the secondary reactions (f_{sec}) estimated for hydrogen events. It was determined that even at the lowest energy, a correction for possible change of charge state is not necessary.

Losses of events due to the dead time of the experiment, mainly due to the acquisition capability, are estimated for each run from the ratio between the free triggers measured on a scaler of high-counting-rate capability and the number of recorded events (or accepted triggers). During the experiment, the counting-rate conditions were kept so that this correction never exceeded 30%, and was most frequently smaller for detection at magnetic rigidities substantially different from the beam rigidity.

An estimation of the global detection efficiency f_ϵ including the detailed analysis of all needed information can be obtained from the difference between the number of accepted triggers and the final number of events that have been analyzed. An event can be analyzed if all the elements required have been registered without any problem: position at the two focal planes, time of flight, and energy loss in the MUSIC detector. The trigger signal obtained by a narrow coincidence on high signals produced by highly ionizing particles is here supposed to identify a true heavy ion with a probability of nearly 100%. In almost all settings, this efficiency was in the range 96–99%.

Corrections due to secondary reactions in the target and in the layers of matter on the trajectory of the fragments (mainly the plastic scintillator of 3 mm thickness at S2) were calculated following the method described in Ref. [30] as previously used in other similar experiments [16]. If a second reaction occurs in the target, the initially produced ion becomes lighter, so cross sections of light ions are artificially increased (and the one for the corresponding heavy ion decreased). If a reaction occurs in the plastic at S2, the spallation ion will most often be out of the narrow magnetic rigidity acceptance in the second part of the FRS and so will be lost at S4. Total nuclear interaction cross sections for the different fragments were estimated using the parametric formula of Kox *et al.* [31]. The maximum value (8%) of this correction factor is obtained for the secondary reactions in the target leading to the lightest evaporation residues. It decreases to zero for heavy residues. The correction due to the loss in the scintillator if a reaction occurs is of the order of 3.5% and was taken into account (as a function of the nature of the ion and of its mean energy). The attenuation of the beam flux inside the finite target thickness was also taken into account in this correction and is equal to −2% for a reaction cross section of 700 mb.

The transmission correction is the most important factor concerning losses in the detection. Because of its geometric characteristics and the ion optics, the FRS has only an angular acceptance of 15 mrad around the beam axis, and a large number of the fragments analyzed in this experiment had an angular distribution at the entrance of the FRS larger than this acceptance. An evaluation of the fraction of the residual yield not detected in the experiment had to be made from the measured velocity distribution of the fragment as described in Ref. [32]. Considering that in the projectile reference frame, the emission of the fragments can be described as a three-dimensional Gaussian distribution around a mean longitudinal recoil, the width of the angular distribution in the laboratory frame can be obtained from the longitudinal velocity distribution measured in the experiment:

$$\sigma(\theta) \approx \frac{\sigma(v_\parallel)}{\langle v_\parallel \rangle}, \quad (3)$$

where $\langle v_\parallel \rangle$ is the mean value, and $\sigma(v_\parallel)$ the width of this distribution for evaporation residues of a given mass.

The transmission through the FRS can be parametrized as

$$T = 1 - \exp\left(-\frac{\alpha_{\mathrm{eff}}(x2, x4)^2}{2\sigma(\theta)^2}\right), \quad (4)$$

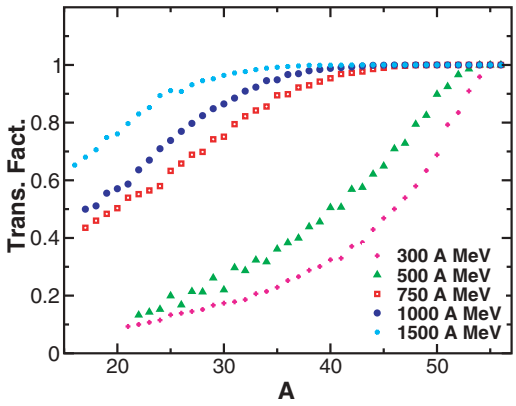

FIG. 4. (Color online) Transmission factor as a function of the mass number of the residue for the five energies presented in this work (see text).

where $\alpha_{\rm eff}(x2, x4)$ is the effective angular acceptance of the FRS as a function of the ion positions $x2$ and $x4$, respectively, at the intermediate S2 and the final focal planes S4. This angle was calculated with the code described in Ref. [32] using 15 mrad as the maximum angular acceptance when the ion optics is the most appropriate.

The transmission factor varies from 1 (no correction) to 0.4 for the lightest fragments that have a much larger angular distribution (see Fig. 4) for the three highest energies. Various reasonable assumptions on the calculation of $\alpha_{\rm eff}(x2, x4)$ lead to uncertainty estimations on T of 1% to 15% for the lightest evaporation residues. However, the analysis has revealed that at 500 and 300A MeV, the magnetic optics settings used during the experiment were not optimal and that the maximum acceptance of the FRS was reduced to 9.15 mrad. This value has been taken into account in the transmission factor leading to much larger corrections for these two energies, as can be seen in Fig. 4.

For the absolute normalization, the precision on the target thickness has been studied in previous experiments [33] and is estimated to be 2.5%. The absolute number of incident ions $N_{{\rm Fe}H}$ and $N_{{\rm Fe}e}$ for runs with the hydrogen target and the empty target, respectively, are obtained from the SEETRAM calibration with an absolute error estimated to be 2.8%.

Experimental values for the isotopic cross sections with their errors are listed in Appendix A. Note that the ^{54}Mn values could not be measured, so they were obtained by a smooth interpolation between the neighboring isotopes and are given in the tables followed by (I). These values are used to obtain integrated quantities as the mass or charge distributions and in the evaluation of the total reaction cross section also given in Appendix A.

Final results of the mean recoil velocity and the width of the velocity distributions for the various residual nuclei are presented in Appendix B. Errors quoted here are due to the velocity reconstruction procedure described above and to the magnetic-rigidity determination. In the case of a truncated velocity distribution, results partially interpolated are followed by (I). The minus sign means that the recoil velocity is opposite to the original direction of the iron beam or, in other words, in the direction of the proton motion in the iron at rest system.

III. RESULTS

A. Isotope production cross sections

Using the experimental method described above, it was possible to measure at five different energies most of the residues produced in the spallation reaction of iron with cross sections larger than 10^{-2} mb, from cobalt ($Z = 27$) down to oxygen ($Z = 8$) or neon ($Z = 10$) depending on the energy. At 1A GeV, cobalt isotopes were not measured.

Figures 5–9 show the isotopic distribution cross sections at the five beam energies. Error bars do not appear, as they are smaller than the data points. The position of the maximum of these isotopic curves is correlated with the excitation energy transferred in the collision between the projectile and the target. In the case of a peripheral collision, in which the excitation energy is limited, only a few particles are evaporated by the fragment, leading to the population of isotopes close to

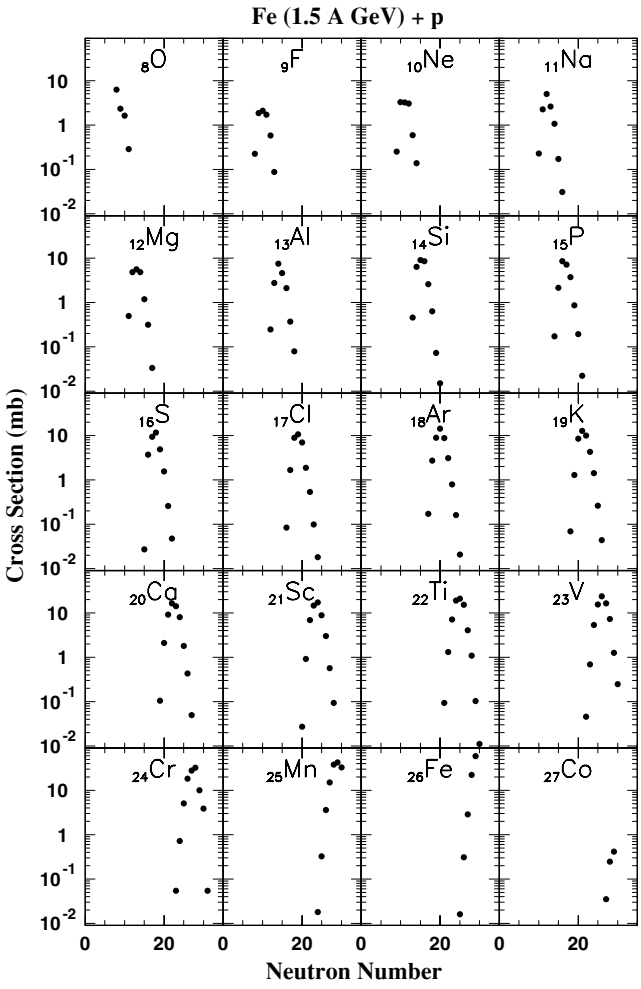

FIG. 5. Isotopic production cross sections of fragments from the reaction ^{56}Fe + p at 1.5A GeV as a function of the neutron number.

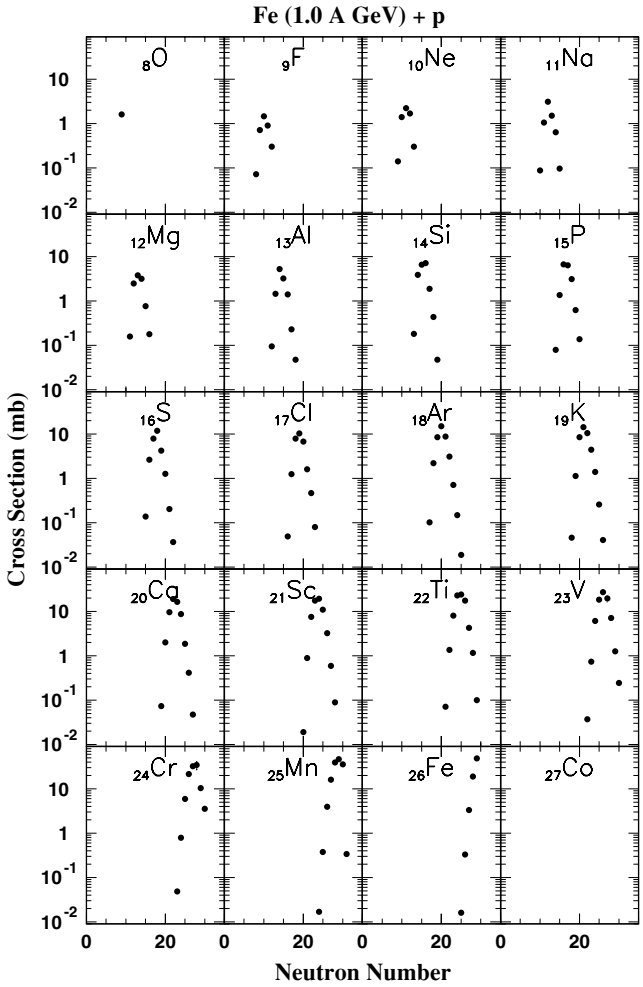

FIG. 6. Same as Fig. 5, but at 1.0*A* GeV.

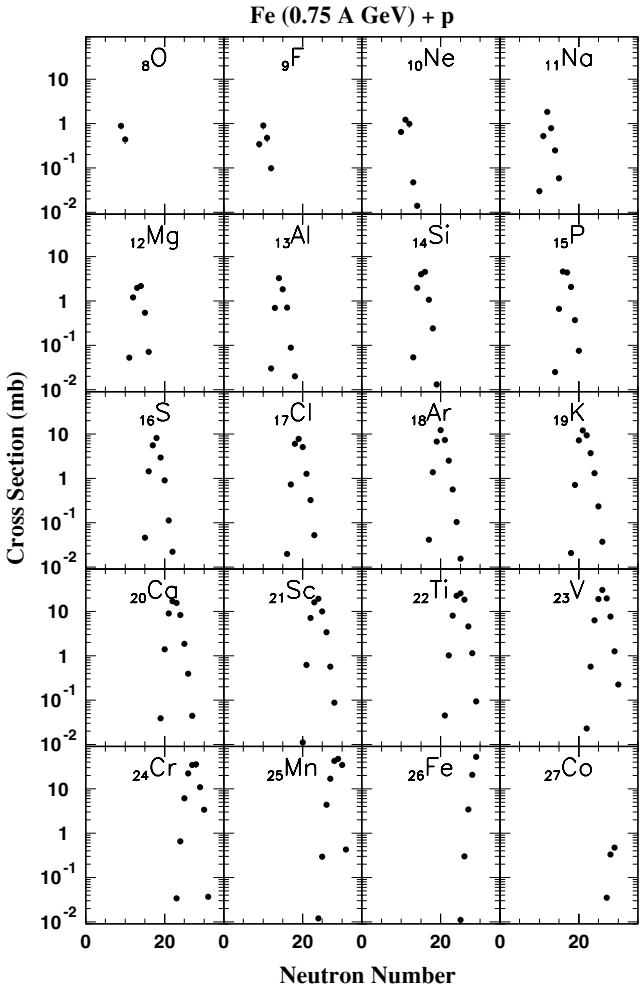

FIG. 7. Same as Fig. 5, but at 0.75*A* GeV.

stability. For more central collisions, the deposited excitation energy is larger, and more neutron-deficient isotopes are produced because of the evaporation phase which favors the emission of neutrons. However, the tendency toward neutron-deficient isotopes is weaker than what is generally observed in heavy systems, because for iron, the Coulomb barrier is much smaller and the neutron-to-proton ratio in the projectile is also smaller.

Isotopic cross sections can be summed to obtain mass or charge distributions. Figure 10 presents the mass distribution of the spallation residues for the five energies of the iron beam analyzed in this experiment. The residues are produced with different cross sections depending on the energy of the projectile. The general trend of the data is globally as expected. As the beam energy increases, the deposited excitation energy becomes more and more important, leading on average to a stronger evaporation of nucleons and finally to lighter evaporation residues. This is reflected by the substantial rise of the light-fragment cross sections between 300 and 1500 MeV per nucleon. As the total reaction cross section is overall rather constant over the studied energy range, this is compensated for by a decrease of the production cross sections of the heaviest evaporation residues with increasing energy. It appears that masses around 46–47 are produced with a cross section almost independent of the beam energy.

B. Comparison with other experimental data

1. Reverse kinematics

The present data can be compared with those obtained by Webber and collaborators using the reverse kinematics method. Measurements were performed on either a thick CH2 target (from $\sim$ 2 to $\sim$ 6g/cm^2) subtracting the carbon contribution [5–7], or a liquid-hydrogen target (1.52g/cm^2) [3,4] at SATURNE. In both cases, the fragments were detected with a telescope of scintillators and Cerenkov counters.

The charge distributions of the spallation residues for several iron beam energies from 330*A* to 1615*A* MeV [4,5,7] have been measured down to Z around 15. In Fig. 11, these results (histograms), at beam energies close to ours, namely, (1512, 1086, 724, 520, and 330)*A* MeV are compared with the present cross sections (symbols) summed over masses to obtain the charge distribution. The overall agreement is satisfying in terms of variation with energy and charge of the residue. A systematic dependence of the element cross

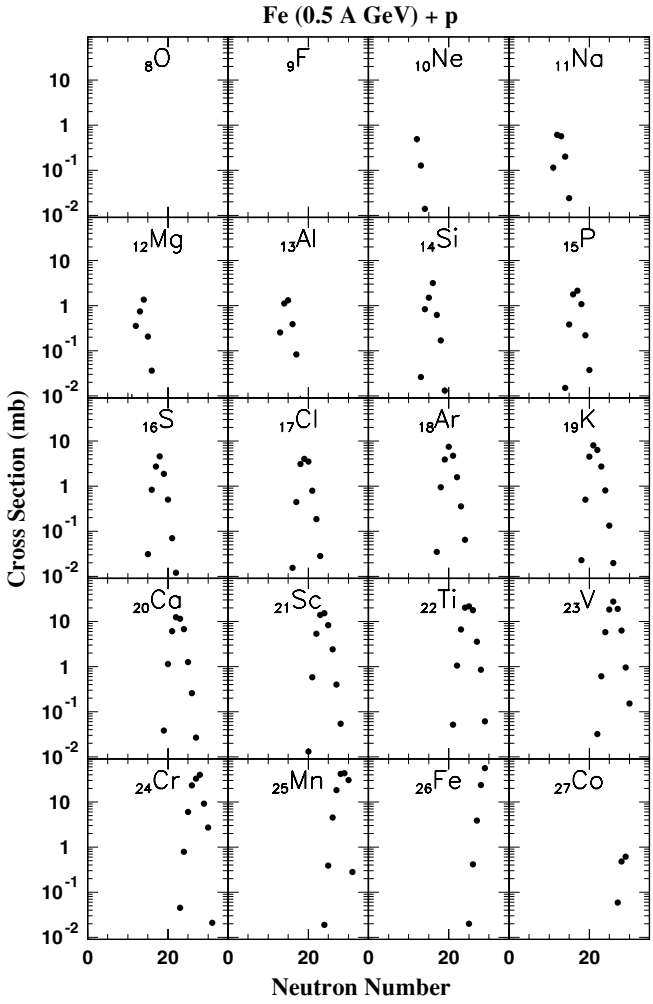

FIG. 8. Same as Fig. 5, but at 0.5A GeV.

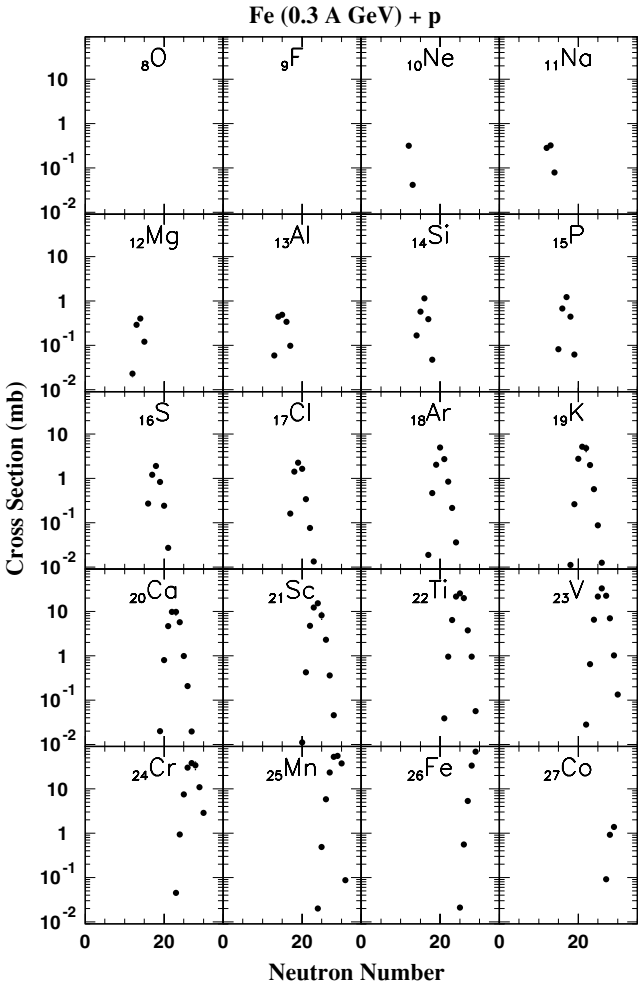

FIG. 9. Same as Fig. 5, but at 0.3A GeV.

sections with the parity of Z is consistently observed in both experiments. The deviation factor, i.e., the average ratio between the two experiments, has been calculated and is shown in Table I. The cross section for $Z = 24$ at 1512A MeV, for which the Webber value is much larger than the neighboring cross sections and inconsistent with a general trend, is excluded. At the three highest energies, it is perfectly compatible with the precisions of both experiments (5% to 20% for Webber *et al*. and 9% to 15% here). At 300A MeV (330A MeV), the discrepancy is larger but still acceptable considering the different energies (10%) of the two measurements. The highest value (1.28) for the deviation factor is found at 500A MeV (520A MeV). Although this could be caused by a particular experimental problem at this energy, it is still compatible within the respective errors, especially if one bears in mind that at low energy, both errors are larger: in our case because of the large transmission correction, and in the case of Webber because of corrections for secondary reactions. The same reasons could explain the fact that for a given energy, the disagreement increases with decreasing Z values, as can be seen in Fig. 11. Another argument is that if we plot charge-changing cross sections as a function of the beam energy for various charges, our results at 500A MeV are ∼10% below a smooth interpolation based on the other

TABLE I. Average ratio of the charge-changing cross sections measured by Webber *et al*. [4,5,7] divided by the values from this experiment.

Energy/nucleon (MeV)	300	500	750	1000	1500
Deviation factor	1.23	1.28	1.01	0.89	0.88

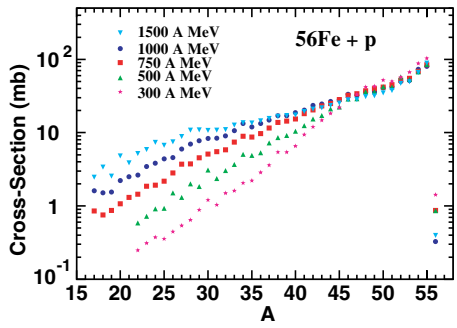

FIG. 10. (Color online) Mass distribution of the residual nuclei in the spallation reaction ^{56}Fe+p at the five different beam energies.

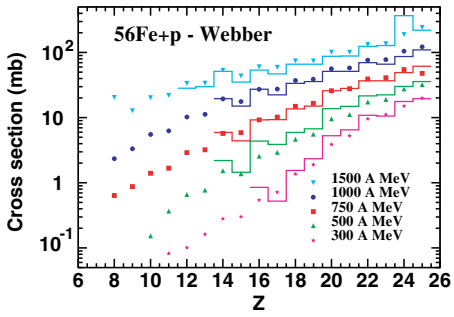

FIG. 11. (Color online) Nuclear-charge distribution of the residual nuclei for the five energies with scaling factors (2/1/0.5/0.25/0.125, respectively, from 1500A to 300A MeV) applied for clarity. Points correspond to the present data, and solid histograms are data from Webber *et al.* [4,5,7] at close energies: (1512, 1086, 724, 520, and 330)A MeV.

measured energies, whereas the Webber values are ∼20% above the interpolation.

The isotopic production cross sections have also been measured previously but only at one energy (573A MeV), using a liquid-hydrogen target [3,4], and were limited to rather large cross sections. The ratios between these values and the present data are displayed in Fig. 12, including the respective

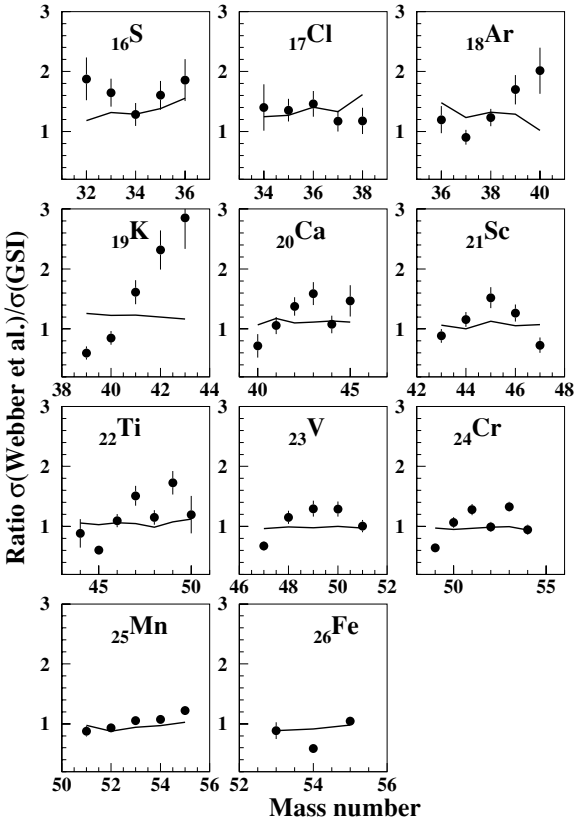

FIG. 12. Ratio between isotopic cross sections measured by Webber *et al.* at 573A MeV [3,4] and the present experiment at 500A MeV for each element as a function of the mass number. Lines are theoretical predictions from INCL4-GEMINI for this ratio.

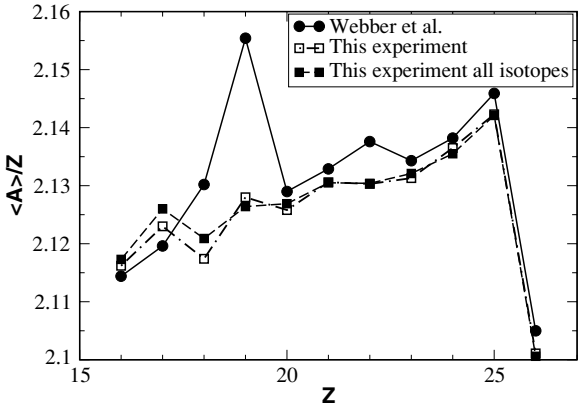

FIG. 13. Ratio of mean nuclear-mass value to the charge for each element measured by Webber *et al.* at 573A MeV [3,4] and in the present experiment at 500A MeV, and for the same quantity evaluated from all isotopes measured in this experiment.

errors. The lines represent the ratios of the cross sections at 573A and 500A MeV computed with the INCL4-GEMINI combination of models. It shows that the difference in energy between the two experiments is not negligible for the lightest fragments, for which it can lead to differences of 30–40%. The agreement between the data is quite good for residues close in mass to iron, but the difference increases for lighter isotopes. The value of the ratio is frequently hardly compatible with the expected value given by the line.

Actually, one would expect a smooth variation of the mean value and of the width of the isotopic distribution with element charge. In Fig. 13 are represented the mean mass-over-charge ratio as the function of Z, summing only the isotopes measured by both experiments. Clearly, these quantities are more fluctuating in the Webber *et al.* experiment, in particular for potassium ($Z = 19$) data and to a smaller extent for argon ($Z = 18$) and titanium ($Z = 22$) ones. The use of our full isotopic distributions, which extend much beyond the ones of Webber *et al.*, does not make a large difference.

2. *Direct kinematics*

Results in direct kinematics have been obtained by Michel and collaborators [2,34,35] by irradiation of natural iron targets at different proton beam energies, allowing the determination of excitation functions from a few tens of MeV to about 2 GeV. Some of the produced residual nuclei have been measured and identified by their γ-ray decay spectrum or by mass spectrometry. These data are compared to our experimental data in Figs. 14 and 15. Results can be split into "cumulative" and "independent" nuclei meaning that they are or are not populated by a decay chain. For cumulative cross sections, our own cross sections have been summed along the decay chain before comparing with Michel's data. The isotopes ^{36}Cl,^{42}K,^{46}Sc,^{48}Sc,^{54}Mn, and ^{52}Fe are independent.

Our data follow quite well, in most cases, the dependence on energy obtained in the Michel *et al.* experiment. This is very satisfying if we consider the difference between the

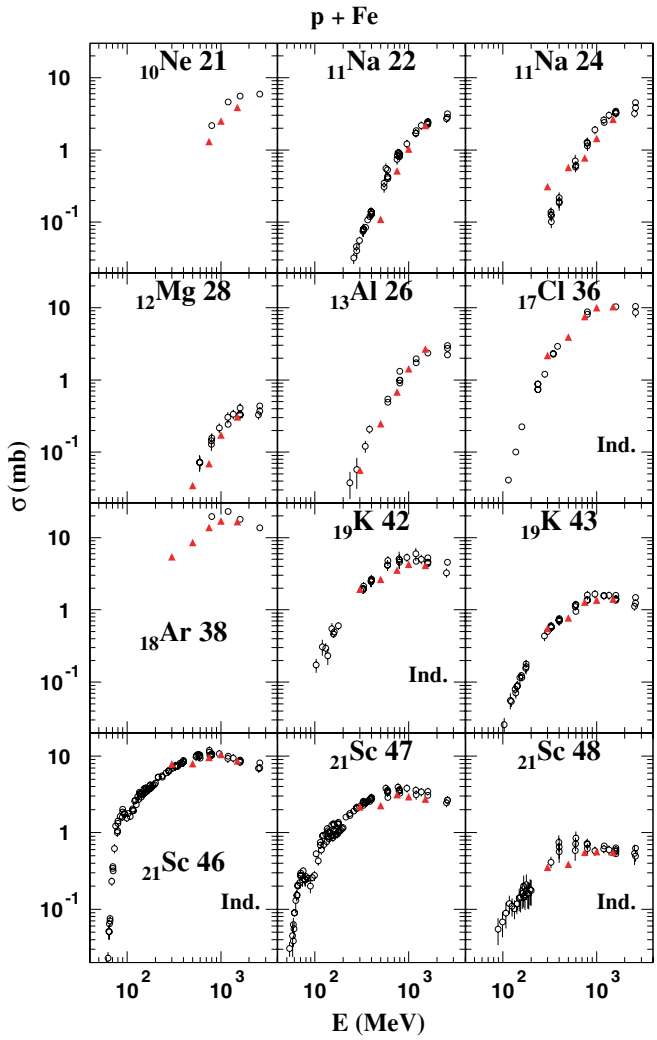

FIG. 14. (Color online) Excitation functions of some residual nuclei produced in the spallation reaction of proton on iron. Open dots are the data of R. Michel *et al.* [34,35] obtained by a direct irradiation; solid triangles correspond to the present experimental data at five energies. Independent isotopes are indicated (Ind.).

two experimental methods. Some of the important differences that can be noticed may be due to the use of natural iron in the case of Michel's data. For instance, the observed higher cross section for ^{52}Fe could come from a contribution of the $(p, 2n)$ reaction on ^{54}Fe adding to the $(p, 4n)$ on ^{56}Fe. Although natural iron is only 6% ^{54}Fe, the effect should be non-negligible, because $(p, 2n)$ is 40 times more probable than $(p, 4n)$ as deduced from our results. Conversely, the lower cross sections found by Michel for ^{52}Mn and the higher one for ^{56}Co at high energy do not seem compatible with the tendency deduced from our isotopic distributions.

Finally, we can say that the present results are qualitatively in good agreement with former measurements. The fact that we have complete isotopic distributions extending down to lighter nuclei than previously measured, on a wide energy range, allows us to check the consistency of our own results and detect possible inconsistencies in other sets of data.

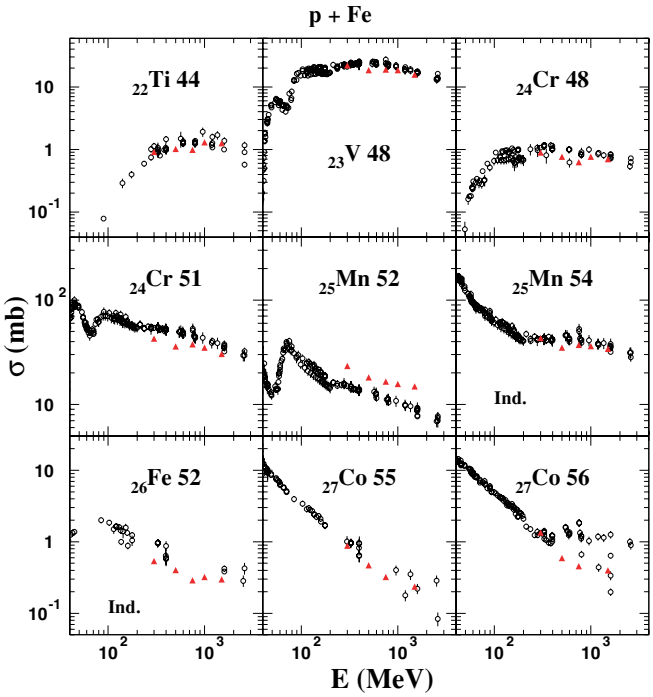

FIG. 15. (Color online) Same as Fig. 14, but for additional nuclei.

C. Comparison with parametric formulas

Since 1950, parametric formulas have been developed by astrophysicists with the aim of predicting the production cross sections of the residual nuclei in spallation reactions. These formulas are used for light and intermediate nuclei present in the composition of the cosmic-rays, such as iron. In this section, we present the comparison of our new experimental data with the results of three of these parametric formulas: Webber [36], EPAX [37], and Silberberg-Tsao [38,39].

1. Webber formula

This parametric formula was developed by Webber *et al.* [36] from the experimental data shown in the previous section. It is used for light spallation residues with $Z_i < 28$ and for energies of the projectile $E > 200$ MeV.

The form of this formula is

$$\sigma(A_i, Z_i, E) = \sigma_0(Z_i, Z_t) f_1(Z_i, A_i, Z_t, A_t) f_2(E, Z_i, Z_t)$$

for residual nuclei (Z_i, A_i) of the spallation reaction on a target nuclei (Z_t, A_t) at energy E, where

$\sigma_0(Z_i, Z_t)$ gives the charge distribution of the residues,

$f_1(Z_i, A_i, Z_t, A_t)$ describes the isotopic curves (from their data at 573 MeV per nucleon), and

$f_2(E, Z_i, Z_t)$ gives the energy dependence.

In Fig. 16, the comparison of our mass distribution with the predictions of the Webber formula is shown. A rather good agreement is obtained at all the energies considered here for the heaviest residues, which are precisely those already measured by Webber *et al.* and used to determine the parameters of

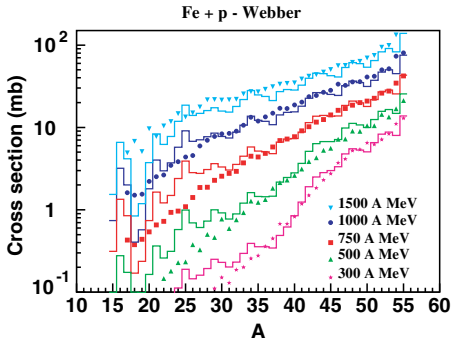

FIG. 16. (Color online) Comparison between present results at five energies (symbols) and the results obtained with the Webber formula (solid lines). Scaling factors (2/1/0.5/0.25/0.125, respectively, from 1500A to 300A MeV) are applied for clarity.

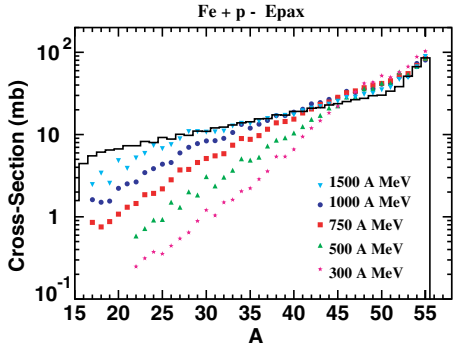

FIG. 17. (Color online) Comparison between the present measured mass distributions (symbols) and the results obtained with the EPAX formula (solid line).

the formula. However, there seems to be some oscillations in the cross sections that are not observed in the data. Actually, the charge distribution, not shown, is more accurately predicted by the formula. This comes from the fact that the isotopic distributions predicted by the Webber formula have smaller widths than those obtained experimentally (see Fig. 19). A probable explanation is that only very few isotopic data were existing when the formula was established. Therefore, the isotopic dependence could not be properly determined. Furthermore, the extrapolation of the parametric formula for light residues that are measured here for the first time shows an important discrepancy with the data. Even if this parametric formula can be useful for determining the production of the most produced spallation residues, this illustrates the danger of using parametric formulas outside the range in which they have been adjusted.

2. *The EPAX formula*

The EPAX formula [37] was created with the aim of describing the production of residues in fragmentation reactions between heavy ions in what is called the *limiting-fragmentation regime* in which the residue production cross section does not depend anymore on the energy of the projectile. Although it is not fully valid for protons at these energies, it might be instructive to know how close its predictions are to the present data. The limiting-fragmentation regime for the spallation reaction Fe+p is expected to be reached for energies of a few GeV per nucleon, so here we can just expect the 1.5A GeV data to be comparable with it.

It can be used for spallation reactions with protons in the case of target nuclei of masses $18<A_t<187$, although it was developed mainly for heavy-ion reactions. The EPAX formula is composed of two factors:

$$\sigma(Z_i, A_i) = Y_A \sigma(Z_{\text{prob}} - Z_i),$$

with Y_A a factor describing the mass distribution of the fragments (Z_i, A_i), that is,

$$Y_A = S_2 \left(A_t^{1/3} + A_{\text{pro}}^{1/3} + S_1\right) P \exp[-P(A_t - A_i)],$$

and $\ln P = P_2 A_t + P_1$. Quantities S_1, S_2, P_1, and P_2 are adjusted parameters, and A_{pro} is the mass of the projectile (one here for protons).

The second factor, $\sigma(Z_{\text{prob}} - Z_i)$, describes the isobaric curves with Z_{prob} as the charge for the maximal production. The various Z_{prob} values as a function of A defines the so-called residue corridor in this approach.

In Fig. 17, our experimental results (symbols) are compared with the predictions of the EPAX formula. The experimental data at 1.5 GeV per nucleon are expected to be the ones closest to the limiting fragmentation regime; therefore, we have renormalized the factor S_2 so that the formula gives the total reaction cross section measured at 1.5 GeV per nucleon (794 mb). Since the EPAX total cross section was 617 mb, this led to a multiplication by 1.28.

It can be seen, as expected, that as the energy increases, the mass distribution gets closer and closer to the EPAX prediction, reaching quite good agreement at 1.5 GeV per nucleon. However, the lightest residues are still overestimated by the formula. The EPAX formula also predicts a more important evaporation of neutrons than seen in the isotopic cross-section data. In fact, the measured N/Z ratio of the residues is higher than that of the residue corridor which is used in the formula.

3. *Silberberg-Tsao formula*

The first version of this parametric formula was developed in 1973 [40] with the experimental data measured by Rudstam [41] concerning the spallation residues in the spallation reaction p+Fe at 340 MeV. Various improvements, especially the beam-energy dependence, have been added in successive versions [38,39]. It can be written as

$$\sigma(A, Z, E) = \sigma_0 f(A)\, f(E)\, e^{-P(E)\Delta A} e^{-R|Z-SA-TA^2|^\nu}\, \Omega\eta\Phi,$$

where

σ_0 is a normalization to the total reaction cross section,

$f(A)$ and $f(E)$ are factors used only in the case of target nuclei $Z_t > 30$,

$e^{-P(E)\Delta A}$ represents the reduction in the production cross section with the mass difference (ΔA) between the residue

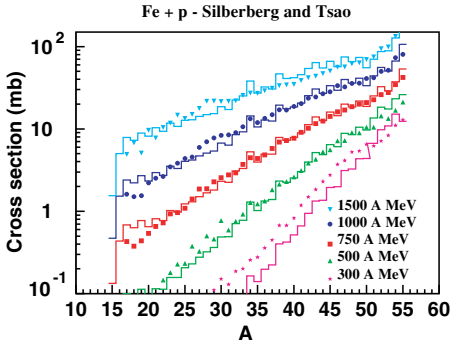

FIG. 18. (Color online) Comparison between present experimental results at the five energies (symbols) and the results obtained with the Silberberg-Tsao formula (solid lines). Scaling factors (2/1/0.5/0.25/0.125, respectively, from 1500A to 300A MeV) are applied for clarity.

and the target nuclei and an energy dependence through the P parameter,

$e^{-R|Z-SA-TA^2|^\nu}$ describes the width and position of the maximum in the isotopic and isobaric production,

Ω takes into account the level structure of the residual nuclei,

η is a factor for the pairing of protons and neutrons, and

Φ represents an increase in the production of very light residues.

In Fig. 18, a comparison of this formula with the experimental results presented in this work is shown. In general, the agreement is very good for all energies between 10% and 30% at 300 MeV per nucleon where the discrepancy is larger.

This last parametric formula appears as the most suitable for reproducing the present data, probably because of the large database used to derive it, which contained systems rather close to the ones studied here. These formulas are quite useful for quickly calculating production rates. Although some physical ingredients are present to derive them, more sophisticated approaches are needed to better handle the physics included in spallation reactions and to describe more fully other observables than cross sections.

4. Isotopic distribution shapes

In the preceding sections, only mass distributions were compared with the predictions of the parametric formulas. But it is also interesting to know how well they reproduce the isotopic distributions. A powerful way to look at this is to compare the shape of the mass distributions of each element through the mean value and width of the mass-over-charge distributions as a function of Z. This is shown in Fig. 19, in which the experimental results at 1500 MeV per nucleon (for better chance of agreement with EPAX) are compared with the three parametric formulas. It can be seen that, as concerns the mean mass-over-charge, the Webber and EPAX formulas agree rather well with the data while the Silberberg-Tsao predicts a slightly too high value. Regarding the widths, EPAX is

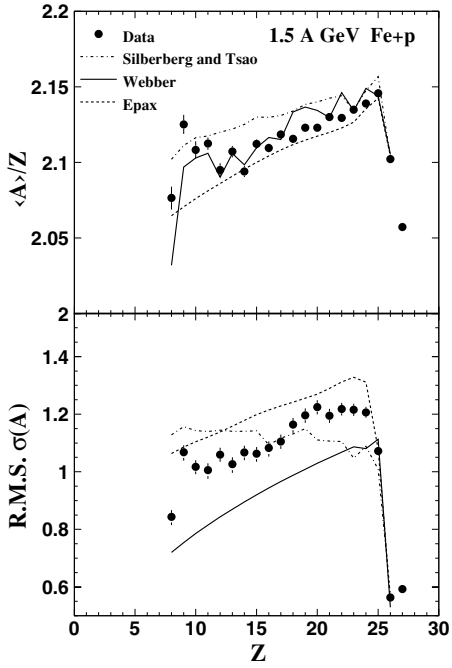

FIG. 19. Mean values and widths of the mass-over-charge distributions as a function of element charge measured at 1500 MeV per nucleon compared with predictions of the Webber, Silberberg-Tsao, and EPAX parametric formulas.

acceptable and Webber tends to produce a too narrow mass distribution, maybe because the formula was fitted on isotopic data that had a rather limited extension. Silberberg-Tsao gives a nearly constant width with Z, in contradiction to the experimental shape. This means that this formula, which gave the best agreement for mass distribution, should be used with caution if one wants to estimate isotope production cross sections.

D. Comparison with models

The design and optimization of spallation sources requires the knowledge of a large number of quantities directly related to spallation reactions in different materials and at various energies. Since exhaustive measurements of such a large amount of data are beyond experimental capabilities, one needs to develop spallation models with good predictability that can be used in transport codes for simulations. This implies a deeper knowledge of the physics of the spallation reactions.

Spallation is generally described by a two-step mechanism. The first stage of the intranuclear cascade (INC) process, governed by nucleon-nucleon collisions, leads to an excited nucleus after the ejection of a few energetic particles (p, n, π, d, α, etc.). The second-longest phase follows corresponding to the evaporative decay of the excited remnant nucleus with a possible competition with fission and Fermi breakup in some cases. Some approaches include also an intermediate stage of preequilibrium to account smoothly for the transition to the full thermalization of the evaporating nucleus.

Old INC models are still currently used in the high-energy transport codes employed for such applications as the

Bertini [42] or ISABEL [43] models. However, recently, a renewed interest for INC models has been triggered by new available spallation data. Among them, one could cite recent improvements on the INC models found in Refs. [44,45]. In the present work, we have compared the experimental results of the spallation residues on iron with the predictions of three INC models: Bertini, ISABEL, and INCL4 [44]. For a long time, the first two ones have been available in transport codes such as LAHET3 [46] and MCNPX [47] for simulations of macrosystems, Bertini (with preequilibrium) being used by default. INCL4 (as well as CEM [45]) was only recently implemented in these code systems. The basic physical assumptions are rather similar, but they differ in their implementation, for instance, the way to develop the *NN* series of interactions, the way to treat Pauli blocking, or the criteria used to stop the INC stage. Note that we have used the implementation of ISABEL in LAHET3 which is blocked above 1 GeV. But this does not means that this cascade is not valid at higher energies.

For the second stage of the reaction, the most commonly used deexcitation model (and default option) in the LAHET and MCNPX codes is the Dresner evaporation model [48] complemented with the Atchison model for fission [49]. It uses the Weisskopf-Ewing formalism [50] for the treatment of the evaporation, as do the more recent models ABLA [51] and GEM [52]. Mainly, these three models differ in the formulas and parameters used to describe the level densities, Coulomb barriers, and inverse reaction cross sections. The Dresner model includes only the evaporation of light particles: neutrons, hydrogen, and helium isotopes. The ABLA model has been mainly tuned for heavy systems, with a particular interest on the fission description. In the version used in this work, only neutrons, protons, and α particles are evaporated. Furthermore, shell and pairing effects as well as γ decay are not taken into account. The GEM model is a recent update of the Dresner model with new parameters, and it extends the Weisskopf-Ewing formalism to the evaporation of intermediate-mass fragments up to $Z = 12$. Actually, the three models (Dresner, ABLA, and GEM) do not take into account in the evaporation process the angular momenta, which in fact are relatively small in spallation reactions induced by incident protons. Fission of heavy systems is described in a Bohr and Wheeler approach using phenomenological fragment distributions in Atchison and GEM. The ABLA approach treats fission as a dynamic process, taking into account the nuclear viscosity, and the fragment distribution is essentially obtained through the calculated population of states above the mass-asymmetric conditional saddle point.

As will be shown in the following, conventional Weisskopf-Ewing evaporation may not be sufficient to account for our data. This is why we will also compare our results with those of models predicting the emission of intermediate-mass fragments through other mechanisms. The GEMINI model [53] treats evaporation of light particles within the Hauser-Feshbach formalism [54], taking explicitly into account the angular momentum. Following the idea of Moretto [55] that there should be a continuous transition between evaporation and fission for all systems including light ones, the emission of intermediate fragments is handled as asymmetric fission in the transition-state model. The transition between Hauser-Feshbach evaporation and asymmetric fission can be chosen through a parameter: in the present work, this parameter has been set so that the transition-state model is used for fragments above helium. Several other options exist in the model. We have used the ones recommended by the author. Some attempts to vary them, although not exhaustive, do not reveal strong differences in the description of the present data.

The SMM model is a numerical implementation of the statistical multifragmentation model from Ref. [56] often used to describe heavy-ion collisions in which multifragmentation is more likely to arise. The parameters used to describe the multifragmentation process are the standard ones as described in Ref. [57]. In particular, the asymptotic freeze-out volume is three times the initial one. The evaporation is treated in the Weisskopf-Ewing formalism up to fragment mass 18, and the lightest primary fragments decays are treated by the Fermi breakup [58].

In the comparison between experimental data and model predictions, it is always difficult to disentangle the respective roles of the intranuclear cascade, which determines the characteristics of the remnant nucleus (charge, mass, angular momentum, and excitation energy) at the end of the cascade stage, and of the deexcitation model. For instance, the under-prediction by the INCL4-ABLA combination of models of the light evaporation residue cross sections observed for heavy systems [18,44] could be ascribed either to a too low excitation energy given by INCL4 or to a deficiency of ABLA at the highest excitation energies. However, some observables can be found that are more sensitive to one reaction stage than to the other. In the following, we will try, as far as possible, to disentangle the influences of the intranuclear cascade and the deexcitation stage in the comparison with the different observables.

1. Total reaction cross section

The total reaction cross section is clearly one of the observables that depends only on the INC model, since it is mainly related to the probability that the incident nucleon makes a collision with one nucleon of the target and that this collision is not blocked by the Pauli principle. In Fig. 20, we present the total reaction cross sections obtained for the five energies analyzed in this work. They were calculated by summing up the isotope productions tabulated in Appendix A. The summation has been done down to $Z = 8$–10 depending on the bombarding energies. The contribution of the unmeasured isotopes was estimated to be at most a few percent, i.e., smaller than the error bars. The fact that the lightest fragments could come from binary breakups and therefore lead to a possible double counting in the total reaction cross section is also negligible. Actually, the two contributions play in opposite directions and even more or less compensate. Previous experimental data from the Barashenkhov compilation [59] are also shown on this figure. A reasonable agreement is observed between most of the previous data and the present ones for both the absolute values and the behavior with the incident energy. The predictions of all three INC models agree with the data within the experimental accuracy, the difference between them being at most 10%.

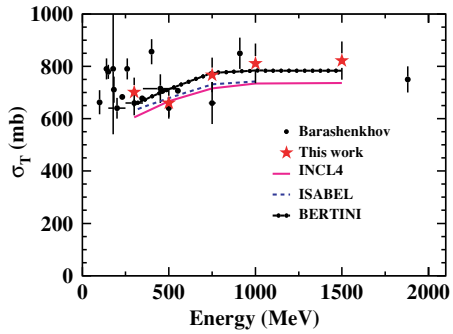

FIG. 20. (Color online) Total reaction cross sections of protons on iron as a function of the bombarding energy (energy per nucleon for this experiment in reverse kinematics). Our five experimental data are compared with the compilation of previous experimental data from Barashenkhov [59] and the values given by the three INC models: Bertini, ISABEL (not available for $E > 1$ GeV in LAHET3), and INCL4.

This is not surprising, since these INC models are known to generally reproduce well the total reaction cross sections at energies above 100 MeV [44,46]. This observable cannot be used to discriminate between these three models.

2. *Mass and charge distributions*

In this section, we examine the various model predictions compared with the mass or charge distributions obtained by summing the measured isotopic cross sections. For completeness, the light-fragment cross sections analyzed in Ref. [29] and obtained during the same experiment are also included at 1 GeV per nucleon.

We first investigate the influence of the choice of the INC model. In Fig. 21, the mass and charge distributions of the residual nuclei produced at 1 GeV are shown and compared with the Bertini intranuclear cascade (plus preequilibrium) followed by the Dresner evaporation. Both mass and charge distributions lead to the same conclusions. The production yields of residues close to iron, which are the major part of the spallation cross section, are underestimated; whereas the yields of intermediate-mass residues are overpredicted. The same conclusions have already been obtained for heavy nuclei [18]. This behavior could be ascribed to a too high excitation energies at the end of the Bertini intranuclear

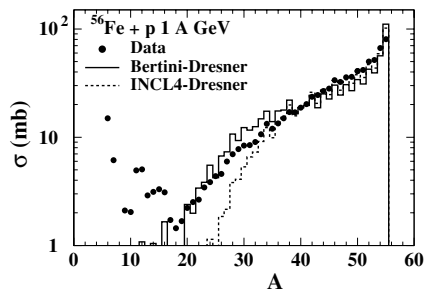

FIG. 21. Mass distribution of the spallation residues of iron at 1A GeV compared with the Bertini and INCL4 INC models combined with the Dresner evaporation model.

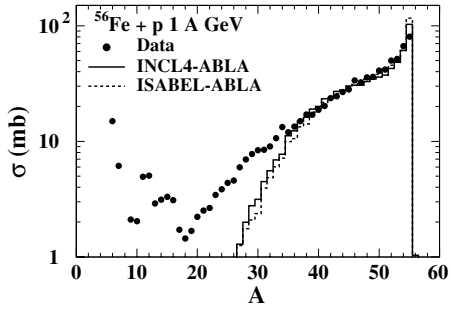

FIG. 22. Mass distribution of the spallation residues of iron at 1A GeV compared with predictions of two different INC models (INCL4 [44] and ISABEL [43]) combined with the ABLA evaporation model [51].

cascade even after the introduction of a preequilibrium phase. A comparison is also shown with INCL4 followed by the same evaporation model. The calculations now predict less excited remnants and a more satisfactory agreement is obtained for the heaviest residues, but the light ones are still underestimated. It can also be noticed that in both cases, the production of very light fragments is greatly underpredicted. Another comparison is shown in Fig. 22 between the mass distribution of the spallation residues and the predictions of two different INC models, ISABEL and INCL4, followed by the ABLA evaporation. This last combination has been shown to reproduce satisfactorily many spallation data [44] in a wide domain and without adjustment of parameters. Both calculations give similar good descriptions of the residues close to iron and underpredict the intermediate and light nuclei cross sections. This underprediction by INCL4-ABLA is in fact consistent with light evaporation residue cross sections obtained from heavier nuclei (lead and gold) [44]. Actually, for the heaviest nuclei, which are mainly formed in peripheral collisions with low excitation energy, evaporation plays a less important role than the intranuclear cascade, since only a very small number of nucleons are evaporated. The fact that both calculations have the same behavior and are rather good for heavy residues suggests that the underprediction of the light residues is not due to a lack of excitation energy. Indeed, we have seen in the comparison with the Bertini model in Fig. 21 that a larger excitation energy does lead to a larger production of light fragments but to the detriment of heavy ones which cannot be counterbalanced by playing with evaporation models. This rather indicates that the problem comes from the deexcitation stage. In the following, we will no longer consider the Bertini model for which many shortcomings have been pointed out [13,18,60]. We will mainly restrict the comparisons to various deexcitation models using INCL4 in the first stage, since ISABEL generally gives similar results.

Figure 23 shows the INCL4 intranuclear cascade coupled with the GEM model, which also takes into account the evaporation of intermediate-mass fragments. The calculated cross sections for the intermediate-mass residues are improved over those obtained by ABLA. However, one observes a slight underestimation of the residues close to iron, and the underprediction of the very light fragments still persists for masses slightly smaller than with ABLA.

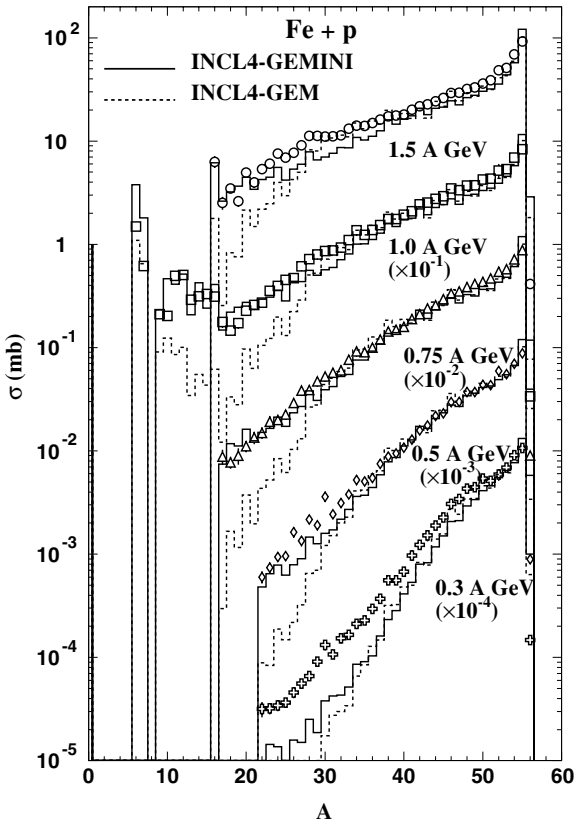

FIG. 23. Spallation residue cross sections of iron as a function of mass number compared with calculations with INCL4 coupled with GEM (dashed lines) or GEMINI (continuous lines). Points are data of the present paper complemented for low masses at 1 GeV by data from Ref. [29] obtained during the same experiment.

From the comparison of the three evaporation models (Dresner, ABLA, and GEM) and the remark concerning excitation energy made above, it can be presumed that standard evaporation models, even including the emission of intermediate-mass fragments (GEM), cannot reproduce the bulk of our data. This is why we tried other models which include other deexcitation modes.

In Fig. 23 are also shown the predictions of GEMINI. If on the heavy fragments the results are slightly less satisfactory than with GEM, the behavior for A lower than 30 is significantly improved. Probably because of its capability of predicting asymmetric fission in the transition-state model prescription, GEMINI appears as the best-suited model for reproducing the bulk of the data except that at the lower energy (300 MeV per nucleon). Actually, at 300 MeV per nucleon, all the calculations, whatever the choice of INC or deexcitation models, start to deviate from experiment around $A = 48$.

Even-odd dissymmetry of the cross sections is clearly visible on an enlarged picture of the Z distribution at 1 GeV per nucleon (Fig. 24) and is representative also of other energies. In spite of a small underprediction of the absolute cross sections with GEMINI, the ratios between odd and even Z cross sections are very close to the experimental ones. Whereas GEM gives a too strong effect, ABLA predicts (with the present version) a slightly too small even-odd effect. But for

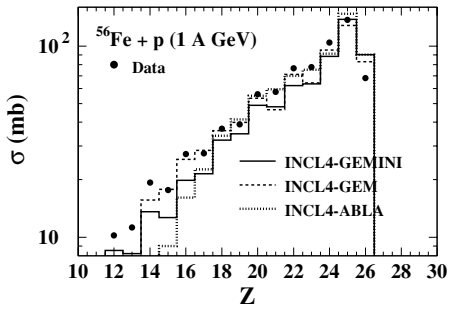

FIG. 24. Charge distribution of the spallation residues of iron at 1A GeV compared with predictions by INCL4 coupled with deexcitation models GEM, GEMINI, and ABLA.

the largest cross sections above 18, the INCL4-ABLA model remains the more precise predictor of the experimental values.

Another mechanism that could be invoked to explain our large yields of light fragments is the onset of multifragmentation at the highest excitation energies [29]. The coupling of INCL4 with the multifragmentation model SMM is shown in Fig. 25. The model describes well the heavy residues and those with masses between 20 and 30. However, it overpredicts the lightest fragments and disagrees strongly with the data in the region $A = 30$–45. The contribution of fragments produced by multifragmentation is shown as the dashed curve in the figure (multifragmentation events being identified by the entry into the multifragmentation routine in the code [61]). The major part of the light-fragment cross section is produced by multifragmentation, while masses above 25 mostly originate from evaporation. However, it is likely that the opening of multifragmentation causes the hole in the region $A = 30$–45, which is not observed experimentally. Our results are at variance with what was found in Ref. [29], where SMM coupled to another INC model (from Ref. [62]) gave good agreement with the data, provided that a preequilibrium stage was added. With INCL4, which, as explained in Ref. [44], handles what is often called the preequilibrium stage, the best agreement with the whole set of data is obtained with GEMINI.

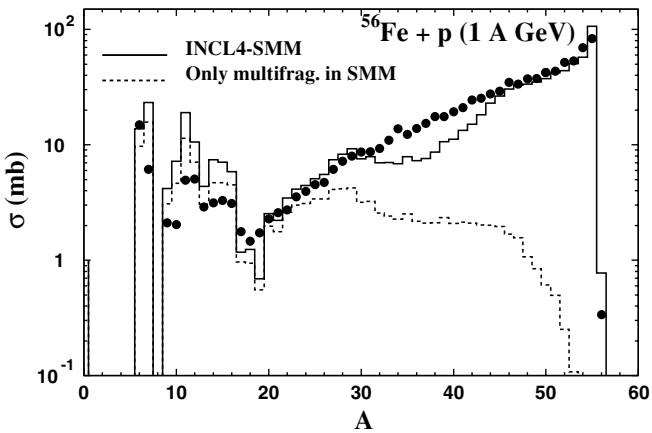

FIG. 25. Cross sections calculated with INCL4 and SMM compared with data points at 1A GeV. Multifragmentation contribution to the calculation is also shown.

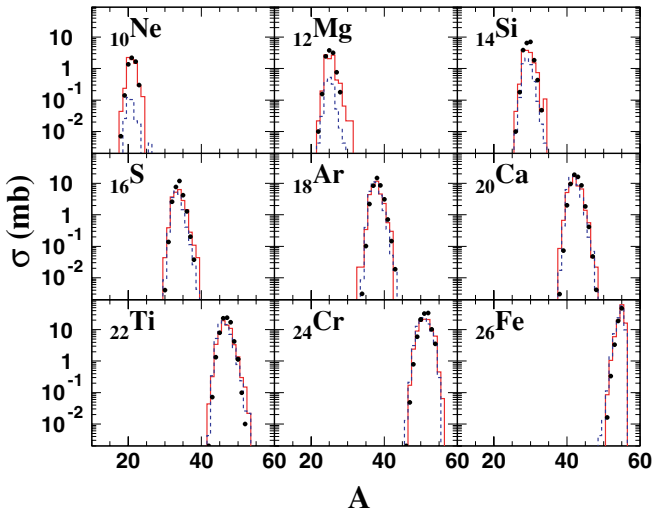

FIG. 26. (Color online) Selected isotopic distributions of cross sections measured at 1A GeV compared with INCL4-GEMINI calculations (continuous lines) and INCL4-ABLA (dashed lines).

However, a clear conclusion regarding the mechanism responsible for the light- and intermediate-fragment production is difficult and would need more constraining information. It seems rather clear that the traditional Weisskopf-Ewing evaporation as used in ABLA or even in GEM, which evaporates intermediate-mass fragments, miss the production of the lightest nuclei. However, the reason for the success of GEMINI, Hauser-Fesbach treatment or asymmetric fission from the transition-state model is not fully understood, and a possible contribution of multifragmentation is not ruled out. Forthcoming exclusive experiments will probably help clarify the situation by identification of the various fragments emitted in coincidence during the deexcitation stage of the reaction.

3. *Isotopic distributions*

In this experiment, more than 500 individual isotopic cross sections were measured and compared systematically with calculations done with the four different deexcitation models (ABLA, GEM, GEMINI, and SMM) coupled with INCL4. As an example, the comparison of GEMINI (full line) and ABLA (dashed line) with a selection of measured isotopic cross sections at 1A GeV is shown on Fig. 26. Except for the better level of cross sections for light residues from GEMINI, already seen when looking at the mass distributions, it is difficult make a conclusion regarding the detailed quality of each model.

A more powerful way to make the comparison is to look at the shapes of the isotopic distributions for each element through the mean atomic mass $\langle A\rangle$ divided by the charge Z of the element and the width (root mean square) of the measured (or computed) distributions. Figure 27 compares these quantities with GEMINI predictions at the five energies, while Fig. 28 shows the results of INCL4 coupled to ABLA, GEM, or SMM at 1A GeV. Actually, it is remarkable that the deviations between models and experiment are qualitatively independent of the beam energy. This can be checked on

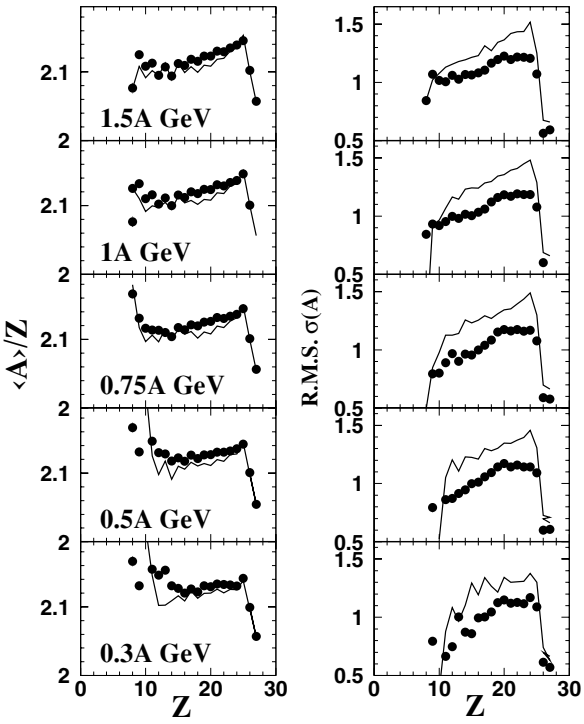

FIG. 27. $\langle A\rangle/Z$ and rms $\sigma(A)$ of the isotopic cross-section distributions as a function of Z, at the five bombarding energies, compared with calculations done with INCL4 coupled with GEMINI. Calculated values have been averaged over the actually measured isotopes.

Fig. 27 for GEMINI but holds also for the comparison with the other models. For this reason, the comparison with the other three models is shown only at 1A GeV in Fig. 28. But again, the following conclusions are the same at all the energies.

For $Z = 25, 26$, and 27 (not measured at 1A GeV), cross sections are dominated by the cascade, leaving the remnant nucleus with very little excitation energy. Therefore, the choice of the evaporation model plays practically no role, and basically the $\langle A\rangle/Z$ is perfectly reproduced. The average value of the isotopic distribution $\langle A\rangle/Z$ is actually very well predicted by GEM and GEMINI over the entire range (down to $Z = 8$–9), with the correct odd-even effects, whereas ABLA gives a value systematically too small. The SMM model gives a correct centroid down to $Z = 20$ but gives the worst prediction below this value, with a distribution centered one mass below the data at lower Z. As for the width of the distributions, no model is good over the entire Z range. The widths computed from GEMINI are systematically a little too wide. With GEM and ABLA, they are too wide only in the range $Z = 20$–25; otherwise, they are very close to the data. For SMM, it is to the contrary, the widths are rather good at high Z but too narrow for lower charges. This fact was already noticed in Ref. [63].

These results show that no deexcitation model is perfect. However, taking into account the information gleaned from observing both the cross sections and the isotopic distribution shapes, we can conclude that the GEMINI model gives the best agreement with our data.

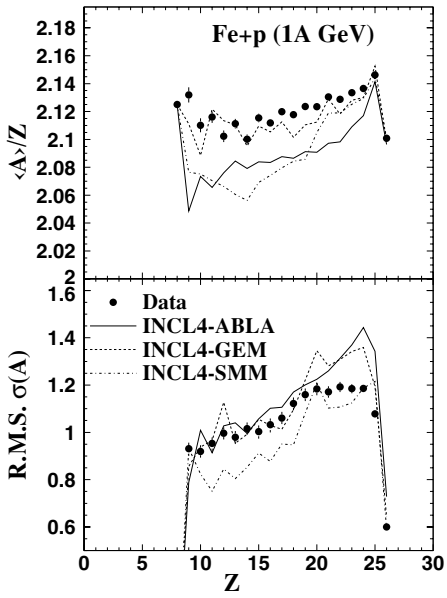

FIG. 28. Same as Fig. 27, but only at 1*A* GeV for comparison with calculations done with INCL4 coupled with ABLA, GEM, and SMM.

4. Recoil velocities

Concerning the kinetic characteristics of the fragments, we show in Fig. 29 a comparison between the experimental mean longitudinal recoil velocities for each mass and those calculated with the INCL4 model combined with ABLA or GEMINI at 1*A* GeV. The same comparison is also done for the width (rms) of the longitudinal distribution.

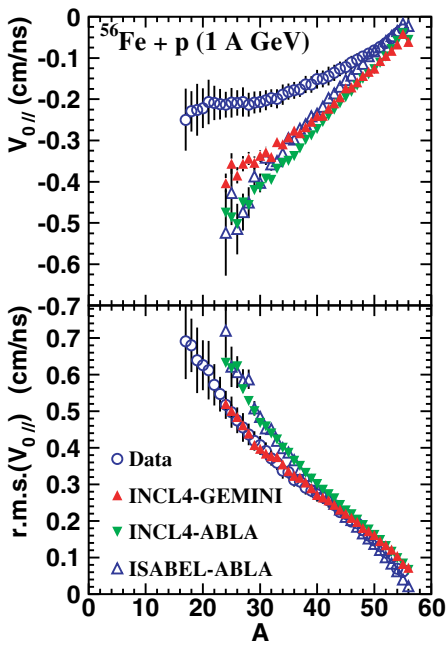

FIG. 29. (Color online) Mean and rms values of the longitudinal recoil velocity distribution for spallation residues at 1*A* GeV vs their atomic mass, comparing experimental values with predictions from INCL4-ABLA, ISABEL-ABLA, and INCL4-GEMINI. Velocities are expressed in the beam (^{56}Fe) rest frame and with a minus sign as being opposite to the iron beam direction.

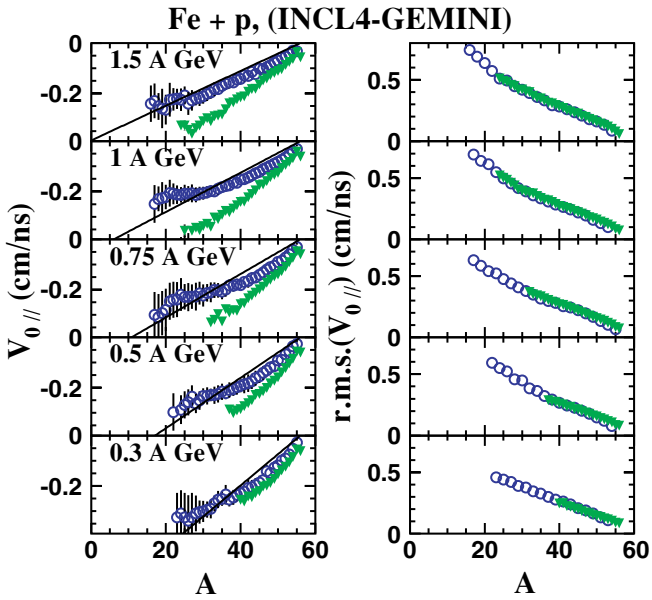

FIG. 30. (Color online) Mean values and rms of the longitudinal recoil velocity distribution for spallation residues vs their atomic mass at all beam energies, comparing experimental values (open circles) with predictions from INCL4-GEMINI (solid triangles). The lines are the Morrissey systematics [64].

One can observe an important discrepancy between the experimental mean recoil velocities and values predicted by the models. It is worthwhile to note that the experimental data decrease much more slowly with decreasing mass than do the values predicted by the models. Furthermore, they seem to saturate at a mass value of 35. This saturation is not seen with ABLA. Only GEMINI shows a clear tendency toward saturation below $A = 30$. For the widths, on the contrary, the agreement with the experimental data is better, especially when using GEMINI. This behavior, presented here at 1 GeV, is very similar at the other energies analyzed in this experiment (Fig. 30). The better agreement with GEMINI could be due to the existence of binary decays in the deexcitation phase that reduce the mean longitudinal velocity of the final residual nuclei, since the recoil momentum will originate from a heavier nucleus and will be split between two partners emitted in an arbitrary direction with respect to the beam direction. In the same figure are also shown the predictions from systematics of Morrisey [64], which more or less give the correct slope for large mass but miss the saturation observed in the data. Actually, the two other deexcitation models, GEM and SMM, not shown here, give results rather similar to ABLA: rather good for the widths but a slope too steep and an inability to describe the saturation of the mean values.

The fact that the mean recoil velocities for the heaviest masses are not well predicted cannot be ascribed to the deexcitation models but should rather raise questions regarding the intranuclear cascade. This is why we also performed a calculation using ISABEL coupled to ABLA, which is presented in Fig. 29. Obviously, ISABEL better reproduces

both the mean values and the widths for masses larger than 50, indicating a possible deficiency of INCL4 in the recoil velocity determination. Actually, a similar systematic deviation of INCL4 concerning the mean velocities has already been noticed for Pb + p at 1A GeV [18]. However, the general trend of the ISABEL calculation over the whole mass range leads to the same conclusion that it is also unable to give the correct slope and saturation effect of the experimental data.

IV. CONCLUSION

The spallation residues produced in the bombardment of ^{56}Fe at (1.5, 1.0, 0.75, 0.5, and 0.3)A GeV on a liquid-hydrogen target have been studied using the reverse kinematics technique and the fragment separator at GSI (Darmstadt). This technique has permitted the full identification in charge and mass of all isotopes produced with cross sections larger than 10^{-2} mb down to $Z = 8$. Their individual production cross sections and recoil velocities at the five energies have been obtained.

The production cross sections have been compared with the previously existing data, either charge-changing cross sections with a few isotopic cross sections at one energy measured in reverse kinematics or excitation functions for a limited number of isotopes obtained by γ spectrometry in direct kinematics. Globally, our results were found to be in good agreement with former data. This comparison also showed that our experimental method leads to a much more complete picture of residue production than what was possible before with the few scattered results, thereby allowing us to sometimes detect possible inconsistencies in other sets of data.

Comparisons with parametric formulas, often used in astrophysics, have been performed. The Webber formula gives rather good predictions of the charge distributions but produces too narrow isotopic distributions. It also totally fails for the lightest nuclei (below $A = 30$–35) in the region not measured at the time when this formula was derived. The EPAX formula (once renormalized to give the correct total reaction cross section) is usable only in the limiting fragmentation regime, apparently not yet fully reached at 1.5A GeV. However, it gives nearly the right A dependence of the cross sections at our highest energy. The best formula seems to be the Silberberg-Tsao, which is in very good agreement with the experimental mass distributions and mean value of the isotopic distributions at all the energies except 300 MeV (as for all the models). The use of parametric formulas can be of great help in making a fast estimation for certain applications, but the example of the Webber formula illustrates the possible danger of using parametric formulas outside the range for which they have been adjusted. Our data could certainly be used to derive new, more reliable parametric formulas for use in cosmic-ray propagation models.

Predictions of different intranuclear-cascade models (Bertini, ISABEL, and INCL4) combined with different deexcitation models (Dresner, ABLA, GEM, SMM, and GEMINI) have been compared with the new experimental data. INCL4 or ISABEL combined with standard Weisskopf-Ewing evaporation models as ABLA or GEM give a good description of the residual production close in charge to iron, but they underpredict systematically the light evaporation residues in the mass region 20–30. This fact, together with the saturation observed in the experimental longitudinal velocity at low masses, could be an indication that another deexcitation mechanism has to be considered. A deexcitation including a possible contribution from multifragmentation, as treated by SMM, improves significantly the predictions of light- and intermediate-mass fragments but at the detriment of residues in the region $A = 30$–45. SMM also misses the saturation of the recoil velocity and does not properly predict the isotopic distribution mean values and widths. The best overall agreement with the data is obtained with the GEMINI model, which gives a rather precise account of all cross sections measured here as a function of the beam energy. The recoil velocities, although not perfect, are the closest to the experimental values, and the mean values and widths of the isotopic distributions are rather well reproduced. Other authors [14,15] have found that GEMINI generally reproduces very well the energy spectra of both light charged particles and intermediate-mass fragments in a wide range of incident energies and target masses. Similar conclusions (best agreement with GEMINI) have been reached in Ref. [65], which used as the INC model the Cascadeexciton model coupled with GEM, GEMINI, and SMM and compared the predictions with the data taken from Ref. [66]. In Ref. [29], with another INC coupled with a preequilibrium stage, the deexcitation model SMM was found to give the best agreement with the 1 GeV data. It is obviously difficult to definitively identify the production mechanism of the intermediate and light mass fragments, and probably only additional experimental information on correlations between residual nuclei and light particles will provide answers to the questions addressed here.

As for the potential interest in using the present data for applications, we supply in Appendixes A and B isotopic cross sections that can be used to directly estimate the change in chemical composition that could occur in an ADS window made predominantly of iron and recoil velocities to calculate damages due to atomic displacements (DPA) [66].

ACKNOWLEDGMENTS

This experiment has benefited from a flexible and efficient operation of the GSI accelerators. Many thanks to all the operating team. The technical support of K. H. Behr, A. Brünle, and K. Burkard was crucial to the preparation of the experimental setup, and the liquid target was smoothly managed by P. Chesny, J. M. Gheller, and G. Guiller. We thank them all for their contributions. Comparison with irradiation experiments (Figs. 14 and 15) was possible thanks to the help of J. C. David and the kindness of Pr. R. Michel in providing us the experimental file. We thank also A. Botvina for helping us identify the multifragmentation contribution in the SMM code. During the interpretation of these results, we benefited greatly from fruitful discussions with J. Cugnon and Y. Yariv.

APPENDIX A

TABLE II. Isotopic cross sections at 1500A MeV, with $\sigma_R = 822 \pm 73$ mb. Interpolated values are indicated as (I), see Sec. II C.

Z	A	σ(mb)	Z	A	σ(mb)	Z	A	σ(mb)	Z	A	σ(mb)	Z	A	σ(mb)
27	54	0.035 ± 0.002	23	52	1.27 ± 0.07	20	48	0.005 ± 0.001	16	33	9.3 ± 1.1	12	24	4.84 ± 0.59
27	55	0.24 ± 0.010	23	53	0.251 ± 0.012	19	37	0.068 ± 0.008	16	34	11.6 ± 1.4	12	25	5.60 ± 0.68
27	56	0.41 ± 0.019	23	54	0.004 ± 0.001	19	38	1.28 ± 0.14	16	35	4.87 ± 0.56	12	26	4.81 ± 0.58
26	51	0.016 ± 0.002	22	43	0.093 ± 0.009	19	39	8.43 ± 0.92	16	36	1.55 ± 0.17	12	27	1.19 ± 0.14
26	52	0.31 ± 0.019	22	44	1.31 ± 0.13	19	40	12.7 ± 1.4	16	37	0.26 ± 0.029	12	28	0.315 ± 0.038
26	53	2.87 ± 0.13	22	45	7.07 ± 0.68	19	41	10.0 ± 1.1	16	38	0.047 ± 0.005	12	29	0.033 ± 0.004
26	54	22.2 ± 0.90	22	46	19.0 ± 1.8	19	42	4.26 ± 0.44	16	39	0.007 ± 0.001	11	21	0.226 ± 0.028
26	55	58.8 ± 2.2	22	47	20.9 ± 1.9	19	43	1.43 ± 0.15	15	29	0.171 ± 0.021	11	22	2.24 ± 0.28
25	49	0.018 ± 0.002	22	48	15.2 ± 2.0	19	44	0.260 ± 0.026	15	30	2.13 ± 0.25	11	23	4.97 ± 0.61
25	50	0.33 ± 0.025	22	49	4.05 ± 0.33	19	45	0.043 ± 0.004	15	31	8.5 ± 1.0	11	24	2.60 ± 0.32
25	51	3.61 ± 0.22	22	50	1.08 ± 0.08	19	46	0.004 ± 0.001	15	32	7.06 ± 0.85	11	25	1.07 ± 0.13
25	52	15.0 ± 0.85	22	51	0.103 ± 0.006	18	35	0.171 ± 0.020	15	33	3.71 ± 0.43	11	26	0.172 ± 0.021
25	53	38.0 ± 1.8	22	52	0.011 ± 0.001	18	36	2.71 ± 0.30	15	34	0.851 ± 0.098	11	27	0.031 ± 0.003
25	54	42.8(I)	21	41	0.027 ± 0.004	18	37	8.8 ± 1.0	15	35	0.193 ± 0.022	10	19	0.253 ± 0.032
25	55	32.9 ± 1.2	21	42	0.92 ± 0.10	18	38	14.1 ± 1.6	15	36	0.022 ± 0.002	10	20	3.23 ± 0.40
24	46	0.002 ± 0.0004	21	43	6.84 ± 0.70	18	39	8.63 ± 0.95	15	37	0.002 ± 0.001	10	21	3.18 ± 0.45
24	47	0.054 ± 0.005	21	44	14.6 ± 1.4	18	40	3.08 ± 0.33	14	27	0.453 ± 0.055	10	22	3.02 ± 0.39
24	48	0.724 ± 0.062	21	45	17.2 ± 1.7	18	41	0.783 ± 0.084	14	28	6.32 ± 0.75	10	23	0.583 ± 0.071
24	49	5.04 ± 0.40	21	46	8.9 ± 1.0	18	42	0.160 ± 0.017	14	29	8.9 ± 1.1	10	24	0.138 ± 0.016
24	50	18.5 ± 1.4	21	47	2.99 ± 0.27	18	43	0.021 ± 0.002	14	30	8.6 ± 1.0	9	17	0.225 ± 0.029
24	51	27.9 ± 1.7	21	48	0.572 ± 0.049	18	44	0.002 ± 0.001	14	31	2.55 ± 0.31	9	18	1.86 ± 0.23
24	52	32.0 ± 4.2	21	49	0.093 ± 0.007	17	33	0.084 ± 0.009	14	32	0.626 ± 0.073	9	19	2.08 ± 0.30
24	53	10.05 ± 0.47	21	50	0.006 ± 0.001	17	34	1.67 ± 0.19	14	33	0.072 ± 0.008	9	20	1.72 ± 0.25
24	54	3.85 ± 0.16	20	39	0.105 ± 0.011	17	35	8.8 ± 1.0	14	34	0.015 ± 0.002	9	21	0.578 ± 0.072
24	55	0.054 ± 0.002	20	40	2.12 ± 0.23	17	36	10.7 ± 1.2	13	25	0.246 ± 0.030	9	22	0.087 ± 0.010
23	45	0.046 ± 0.004	20	41	9.20 ± 0.98	17	37	6.96 ± 0.82	13	26	2.75 ± 0.33	8	16	6.28 ± 0.80
23	46	0.693 ± 0.064	20	42	16.3 ± 1.7	17	38	1.87 ± 0.21	13	27	7.47 ± 0.89	8	17	2.30 ± 0.36
23	47	5.37 ± 0.48	20	43	14.3 ± 1.5	17	39	0.536 ± 0.059	13	28	4.55 ± 0.55	8	18	1.63 ± 0.27
23	48	15.4 ± 1.3	20	44	8.06 ± 0.80	17	40	0.098 ± 0.010	13	29	2.09 ± 0.33	8	19	0.285 ± 0.035
23	49	23.7 ± 1.9	20	45	1.81 ± 0.17	17	41	0.018 ± 0.002	13	30	0.366 ± 0.043			
23	50	16.3 ± 2.4	20	46	0.426 ± 0.039	16	31	0.027 ± 0.003	13	31	0.078 ± 0.009			
23	51	7.18 ± 0.45	20	47	0.050 ± 0.004	16	32	3.68 ± 0.43	12	23	0.498 ± 0.061			

TABLE III. Same as Table II, but at 1000A MeV, with $\sigma_R = 811 \pm 76$ mb.

Z	A	σ(mb)	Z	A	σ(mb)	Z	A	σ(mb)	Z	A	σ(mb)	Z	A	σ(mb)
26	51	0.016 ± 0.001	23	53	0.246 ± 0.011	20	46	0.416 ± 0.038	16	30	0.004 ± 0.001	13	30	0.229 ± 0.027
26	52	0.333 ± 0.019	23	54	0.004 ± 0.001	20	47	0.048 ± 0.004	16	31	0.138 ± 0.017	13	31	0.047 ± 0.005
26	53	3.32 ± 0.16	22	42	0.002 ± 0.001	20	48	0.004 ± 0.001	16	32	2.61 ± 0.31	12	22	0.010 ± 0.001
26	54	18.98 ± 0.77	22	43	0.071 ± 0.007	19	37	0.046 ± 0.005	16	33	7.80 ± 0.90	12	23	0.158 ± 0.020
26	55	48.0 ± 1.8	22	44	1.35 ± 0.13	19	38	1.12 ± 0.12	16	34	11.9 ± 1.6	12	24	2.48 ± 0.31
25	49	0.017 ± 0.001	22	45	8.00 ± 0.76	19	39	8.34 ± 0.91	16	35	4.21 ± 0.50	12	25	3.79 ± 0.46
25	50	0.37 ± 0.028	22	46	22.7 ± 2.1	19	40	14.1 ± 1.5	16	36	1.27 ± 0.14	12	26	3.16 ± 0.38
25	51	3.97 ± 0.25	22	47	24.1 ± 2.2	19	41	10.6 ± 1.2	16	37	0.202 ± 0.023	12	27	0.760 ± 0.092
25	52	15.93 ± 0.90	22	48	17.5 ± 2.4	19	42	4.41 ± 0.49	16	38	0.037 ± 0.004	12	28	0.178 ± 0.022
25	53	39.6 ± 1.8	22	49	4.25 ± 0.34	19	43	1.40 ± 0.14	15	28	0.004 ± 0.001	11	20	0.009 ± 0.001
25	54	46.7(I)	22	50	1.162 ± 0.086	19	44	0.257 ± 0.026	15	29	0.078 ± 0.009	11	21	0.087 ± 0.011
25	55	35.4 ± 1.3	22	51	0.100 ± 0.006	19	45	0.040 ± 0.004	15	30	1.36 ± 0.16	11	22	1.05 ± 0.13
25	56	0.34 ± 0.01	22	52	0.010 ± 0.001	18	34	0.003 ± 0.001	15	31	6.67 ± 0.78	11	23	3.09 ± 0.39

TABLE III. *(Continued.)*

Z	A	σ(mb)	Z	A	σ(mb)	Z	A	σ(mb)	Z	A	σ(mb)	Z	A	σ(mb)
24	46	0.002 ± 0.001	21	41	0.019 ± 0.002	18	35	0.101 ± 0.011	15	32	6.28 ± 0.93	11	24	1.48 ± 0.22
24	47	0.048 ± 0.0041	21	42	0.882 ± 0.091	18	36	2.22 ± 0.25	15	33	3.07 ± 0.36	11	25	0.629 ± 0.076
24	48	0.789 ± 0.067	21	43	7.43 ± 0.76	18	37	8.42 ± 0.94	15	34	0.623 ± 0.072	11	26	0.096 ± 0.011
24	49	5.93 ± 0.47	21	44	17.4 ± 1.7	18	38	14.8 ± 1.6	15	35	0.137 ± 0.016	10	18	0.007 ± 0.001
24	50	21.3 ± 1.6	21	45	19.2 ± 1.8	18	39	8.66 ± 0.99	14	26	0.010 ± 0.001	10	19	0.140 ± 0.019
24	51	32.2 ± 2.0	21	46	10.9 ± 1.5	18	40	3.11 ± 0.33	14	27	0.180 ± 0.022	10	20	1.38 ± 0.18
24	52	34.2 ± 8.1	21	47	3.20 ± 0.29	18	41	0.714 ± 0.076	14	28	3.85 ± 0.46	10	21	2.20 ± 0.28
24	53	10.34 ± 0.48	21	48	0.586 ± 0.050	18	42	0.148 ± 0.016	14	29	6.53 ± 0.77	10	22	1.66 ± 0.21
24	54	3.56 ± 0.14	21	49	0.089 ± 0.007	18	43	0.019 ± 0.002	14	30	7.04 ± 0.83	10	23	0.299 ± 0.038
23	44	0.002 ± 0.001	21	50	0.005 ± 0.001	17	32	0.003 ± 0.001	14	31	1.87 ± 0.23	9	17	0.072 ± 0.009
23	45	0.037 ± 0.003	20	38	0.003 ± 0.001	17	33	0.049 ± 0.005	14	32	0.431 ± 0.051	9	18	0.706 ± 0.094
23	46	0.736 ± 0.068	20	39	0.074 ± 0.008	17	34	1.25 ± 0.15	14	33	0.047 ± 0.005	9	19	1.45 ± 0.20
23	47	6.10 ± 0.55	20	40	2.01 ± 0.22	17	35	7.89 ± 0.90	13	24	0.006 ± 0.001	9	20	0.89 ± 0.12
23	48	18.3 ± 1.6	20	41	9.7 ± 1.0	17	36	10.3 ± 1.2	13	25	0.094 ± 0.011	9	21	0.300 ± 0.037
23	49	27.1 ± 2.2	20	42	19.0 ± 2.0	17	37	6.73 ± 0.81	13	26	1.45 ± 0.17	8	17	1.59 ± 0.21
23	50	19.6 ± 3.7	20	43	16.4 ± 2.0	17	38	1.61 ± 0.18	13	27	5.20 ± 0.63			
23	51	7.11 ± 0.44	20	44	8.65 ± 0.90	17	39	0.464 ± 0.051	13	28	3.17 ± 0.38			
23	52	1.259 ± 0.071	20	45	1.87 ± 0.18	17	40	0.080 ± 0.008	13	29	1.39 ± 0.17			

TABLE IV. Same as Table II, but at 750A MeV, with $\sigma_R = 767 \pm 66$ mb.

Z	A	σ(mb)	Z	A	σ(mb)	Z	A	σ(mb)	Z	A	σ(mb)	Z	A	σ(mb)
27	54	0.035 ± 0.002	23	50	19.7 ± 2.5	20	44	8.33 ± 0.83	17	39	0.322 ± 0.035	13	28	1.84 ± 0.23
27	55	0.333 ± 0.015	23	51	7.65 ± 0.47	20	45	1.86 ± 0.18	17	40	0.052 ± 0.005	13	29	0.714 ± 0.087
27	56	0.474 ± 0.023	23	52	1.270 ± 0.073	20	46	0.390 ± 0.036	16	31	0.046 ± 0.006	13	30	0.088 ± 0.010
26	51	0.011 ± 0.001	23	53	0.225 ± 0.010	20	47	0.045 ± 0.004	16	32	1.44 ± 0.17	13	31	0.020 ± 0.002
26	52	0.300 ± 0.018	23	54	0.003 ± 0.001	20	48	0.004 ± 0.001	16	33	5.54 ± 0.64	12	23	0.052 ± 0.008
26	53	3.44 ± 0.17	22	43	0.045 ± 0.004	19	37	0.021 ± 0.002	16	34	8.11 ± 0.94	12	24	1.19 ± 0.15
26	54	20.84 ± 0.84	22	44	1.02 ± 0.10	19	38	0.714 ± 0.079	16	35	2.92 ± 0.34	12	25	1.97 ± 0.25
26	55	52.8 ± 2.0	22	45	7.98 ± 0.76	19	39	7.27 ± 0.79	16	36	0.90 ± 0.10	12	26	2.15 ± 0.28
25	49	0.012 ± 0.001	22	46	22.4 ± 2.1	19	40	12.0 ± 1.3	16	37	0.11 ± 0.012	12	27	0.54 ± 0.071
25	50	0.298 ± 0.020	22	47	25.3 ± 2.3	19	41	9.3 ± 1.1	16	38	0.022 ± 0.002	12	28	0.071 ± 0.008
25	51	4.37 ± 0.27	22	48	18.3 ± 1.8	19	42	3.65 ± 0.38	16	39	0.003 ± 0.001	12	29	0.002 ± 0.001
25	52	16.83 ± 0.95	22	49	4.58 ± 0.37	19	43	1.31 ± 0.13	15	29	0.025 ± 0.003	11	21	0.030 ± 0.005
25	53	42.7 ± 2.0	22	50	1.145 ± 0.085	19	44	0.231 ± 0.023	15	30	0.664 ± 0.080	11	22	0.526 ± 0.085
25	54	47.1(I)	22	51	0.093 ± 0.006	19	45	0.037 ± 0.003	15	31	4.57 ± 0.54	11	23	1.81 ± 0.25
25	55	34.5 ± 1.3	22	52	0.009 ± 0.001	19	46	0.003 ± 0.001	15	32	4.35 ± 0.64	11	24	0.78 ± 0.10
25	56	0.429 ± 0.020	21	41	0.011 ± 0.001	18	35	0.041 ± 0.005	15	33	2.07 ± 0.25	11	25	0.249 ± 0.031
24	47	0.034 ± 0.003	21	42	0.619 ± 0.064	18	36	1.38 ± 0.16	15	34	0.368 ± 0.043	11	26	0.058 ± 0.007
24	48	0.653 ± 0.056	21	43	7.05 ± 0.72	18	37	6.78 ± 0.76	15	35	0.074 ± 0.008	10	20	0.64 ± 0.10
24	49	6.14 ± 0.50	21	44	16.2 ± 1.6	18	38	12.3 ± 1.4	15	36	0.005 ± 0.001	10	21	1.22 ± 0.18
24	50	22.3 ± 1.7	21	45	19.4 ± 1.9	18	39	7.28 ± 0.82	14	27	0.053 ± 0.008	10	22	0.97 ± 0.17
24	51	34.6 ± 2.1	21	46	10.0 ± 1.0	18	40	2.49 ± 0.27	14	28	1.96 ± 0.23	10	23	0.047 ± 0.007
24	52	35.7 ± 6.1	21	47	3.40 ± 0.30	18	41	0.559 ± 0.060	14	29	3.96 ± 0.48	10	24	0.014 ± 0.002
24	53	10.96 ± 0.51	21	48	0.575 ± 0.049	18	42	0.103 ± 0.010	14	30	4.51 ± 0.54	9	18	0.342 ± 0.057
24	54	3.41 ± 0.14	21	49	0.087 ± 0.007	18	43	0.016 ± 0.002	14	31	1.06 ± 0.13	9	19	0.90 ± 0.16
24	55	0.037 ± 0.002	21	50	0.005 ± 0.001	17	33	0.020 ± 0.002	14	32	0.239 ± 0.028	9	20	0.469 ± 0.088
23	45	0.023 ± 0.002	20	39	0.039 ± 0.004	17	34	0.721 ± 0.084	14	33	0.013 ± 0.002	9	21	0.097 ± 0.014
23	46	0.569 ± 0.053	20	40	1.39 ± 0.15	17	35	5.98 ± 0.69	14	34	0.004 ± 0.001	8	17	0.88 ± 0.15
23	47	6.34 ± 0.57	20	41	8.99 ± 0.96	17	36	7.73 ± 0.87	13	25	0.030 ± 0.004	8	18	0.431 ± 0.083
23	48	18.9 ± 1.6	20	42	16.7 ± 1.7	17	37	5.08 ± 0.58	13	26	0.702 ± 0.087			
23	49	30.5 ± 2.4	20	43	15.6 ± 1.7	17	38	1.27 ± 0.14	13	27	3.24 ± 0.42			

TABLE V. Same as Table II, but at 500A MeV, with $\sigma_R = 660 \pm 53$ mb.

Z	A	σ(mb)	Z	A	σ(mb)	Z	A	σ(mb)	Z	A	σ(mb)	Z	A	σ(mb)
27	53	0.003 ± 0.001	23	47	5.83 ± 0.52	20	39	0.038 ± 0.004	17	33	0.015 ± 0.002	14	31	0.614 ± 0.079
27	54	0.059 ± 0.002	23	48	18.3 ± 1.6	20	40	1.15 ± 0.12	17	34	0.442 ± 0.051	14	32	0.167 ± 0.020
27	55	0.485 ± 0.020	23	49	27.5 ± 2.6	20	41	6.15 ± 0.66	17	35	3.12 ± 0.36	14	33	0.013 ± 0.002
27	56	0.611 ± 0.025	23	50	19.0 ± 2.7	20	42	12.5 ± 1.3	17	36	4.02 ± 0.50	13	25	0.008 ± 0.001
26	51	0.020 ± 0.001	23	51	6.27 ± 0.39	20	43	11.4 ± 1.4	17	37	3.52 ± 0.43	13	26	0.254 ± 0.032
26	52	0.416 ± 0.024	23	52	0.949 ± 0.054	20	44	6.72 ± 0.75	17	38	0.787 ± 0.087	13	27	1.11 ± 0.15
26	53	3.86 ± 0.18	23	53	0.152 ± 0.007	20	45	1.26 ± 0.12	17	39	0.188 ± 0.021	13	28	1.31 ± 0.17
26	54	23.51 ± 0.94	23	54	0.002 ± 0.001	20	46	0.256 ± 0.024	17	40	0.028 ± 0.003	13	29	0.383 ± 0.050
26	55	56.6 ± 2.1	22	43	0.052 ± 0.005	20	47	0.027 ± 0.002	16	31	0.031 ± 0.004	13	30	0.083 ± 0.010
25	49	0.019 ± 0.002	22	44	1.05 ± 0.10	20	48	0.002 ± 0.001	16	32	0.822 ± 0.097	13	31	0.009 ± 0.001
25	50	0.387 ± 0.029	22	45	6.65 ± 0.64	19	37	0.023 ± 0.003	16	33	2.69 ± 0.31	12	23	0.009 ± 0.002
25	51	4.49 ± 0.28	22	46	20.5 ± 1.9	19	38	0.501 ± 0.056	16	34	4.57 ± 0.58	12	24	0.354 ± 0.044
25	52	18.3 ± 1.0	22	47	21.5 ± 2.2	19	39	4.48 ± 0.49	16	35	1.86 ± 0.23	12	25	0.748 ± 0.093
25	53	42.0 ± 1.9	22	48	17.7 ± 2.2	19	40	8.00 ± 0.86	16	36	0.499 ± 0.057	12	26	1.36 ± 0.19
25	54	43.3(I)	22	49	3.53 ± 0.28	19	41	6.33 ± 0.76	16	37	0.070 ± 0.008	12	27	0.206 ± 0.028
25	55	30.8 ± 1.1	22	50	0.864 ± 0.064	19	42	2.71 ± 0.31	16	38	0.012 ± 0.001	12	28	0.036 ± 0.004
25	56	0.280 ± 0.011	22	51	0.061 ± 0.004	19	43	0.795 ± 0.081	15	29	0.015 ± 0.002	11	22	0.113 ± 0.018
24	47	0.045 ± 0.004	22	52	0.005 ± 0.001	19	44	0.134 ± 0.013	15	30	0.378 ± 0.045	11	23	0.607 ± 0.085
24	48	0.792 ± 0.067	21	41	0.013 ± 0.002	19	45	0.020 ± 0.002	15	31	1.78 ± 0.21	11	24	0.570 ± 0.077
24	49	5.98 ± 0.48	21	42	0.581 ± 0.061	18	35	0.035 ± 0.004	15	32	2.13 ± 0.27	11	25	0.199 ± 0.025
24	50	23.2 ± 1.7	21	43	5.37 ± 0.55	18	36	0.95 ± 0.11	15	33	1.08 ± 0.14	11	26	0.024 ± 0.003
24	51	32.5 ± 2.0	21	44	13.9 ± 1.4	18	37	3.88 ± 0.43	15	34	0.219 ± 0.026	10	22	0.487 ± 0.080
24	52	39.8 ± 3.6	21	45	15.1 ± 1.6	18	38	7.51 ± 0.83	15	35	0.037 ± 0.004	10	23	0.125 ± 0.017
24	53	9.19 ± 0.43	21	46	8.24 ± 0.92	18	39	4.74 ± 0.57	15	36	0.003 ± 0.001	10	24	0.014 ± 0.002
24	54	2.73 ± 0.11	21	47	2.41 ± 0.22	18	40	1.59 ± 0.19	14	27	0.026 ± 0.004			
24	55	0.021 ± 0.001	21	48	0.397 ± 0.034	18	41	0.356 ± 0.038	14	28	0.819 ± 0.098			
23	45	0.032 ± 0.003	21	49	0.054 ± 0.004	18	42	0.064 ± 0.006	14	29	1.50 ± 0.18			
23	46	0.614 ± 0.057	21	50	0.002 ± 0.001	18	43	0.008 ± 0.001	14	30	3.15 ± 0.41			

TABLE VI. Same as Table II, but at 300A MeV, with $\sigma_R = 701 \pm 56$ mb.

Z	A	σ(mb)	Z	A	σ(mb)	Z	A	σ(mb)	Z	A	σ(mb)	Z	A	σ(mb)
27	54	0.092 ± 0.004	23	46	0.640 ± 0.060	21	48	0.363 ± 0.031	18	40	0.837 ± 0.091	15	34	0.062 ± 0.007
27	55	0.913 ± 0.034	23	47	6.50 ± 0.58	21	49	0.046 ± 0.004	18	41	0.213 ± 0.023	15	35	0.010 ± 0.001
27	56	1.390 ± 0.054	23	48	21.8 ± 1.9	21	50	0.002 ± 0.001	18	42	0.036 ± 0.004	14	28	0.165 ± 0.020
26	51	0.021 ± 0.001	23	49	33.2 ± 2.7	20	39	0.020 ± 0.002	18	43	0.004 ± 0.001	14	29	0.571 ± 0.069
26	52	0.554 ± 0.031	23	50	22.3 ± 2.4	20	40	0.798 ± 0.086	17	33	0.006 ± 0.001	14	30	1.15 ± 0.15
26	53	5.31 ± 0.25	23	51	6.94 ± 0.43	20	41	4.65 ± 0.50	17	34	0.160 ± 0.019	14	31	0.386 ± 0.051
26	54	33.0 ± 1.3	23	52	1.014 ± 0.057	20	42	9.9 ± 1.0	17	35	1.43 ± 0.16	14	32	0.047 ± 0.006
26	55	68.4 ± 2.5	23	53	0.133 ± 0.006	20	43	9.8 ± 1.8	17	36	2.24 ± 0.26	14	33	0.005 ± 0.001
25	49	0.020 ± 0.002	23	54	0.0006 ± 0.00008	20	44	5.74 ± 0.64	17	37	1.63 ± 0.20	13	26	0.059 ± 0.007
25	50	0.495 ± 0.037	22	43	0.039 ± 0.004	20	45	0.986 ± 0.094	17	38	0.339 ± 0.038	13	27	0.438 ± 0.059
25	51	5.86 ± 0.36	22	44	0.942 ± 0.093	20	46	0.206 ± 0.020	17	39	0.076 ± 0.008	13	28	0.491 ± 0.067
25	52	23.5 ± 1.3	22	45	6.41 ± 0.61	20	47	0.020 ± 0.002	17	40	0.013 ± 0.001	13	29	0.334 ± 0.044
25	53	52.5 ± 2.4	22	46	21.6 ± 2.0	19	37	0.011 ± 0.001	17	41	0.002 ± 0.001	13	30	0.098 ± 0.013
25	54	55.0(I)	22	47	25.2 ± 2.3	19	38	0.261 ± 0.029	16	31	0.006 ± 0.001	13	31	0.004 ± 0.001
25	55	37.7 ± 1.4	22	48	20.1 ± 2.0	19	39	2.77 ± 0.30	16	32	0.271 ± 0.032	12	24	0.023 ± 0.004
25	56	0.088 ± 0.004	22	49	3.76 ± 0.30	19	40	5.13 ± 0.55	16	33	1.20 ± 0.14	12	25	0.288 ± 0.037
24	47	0.045 ± 0.004	22	50	0.949 ± 0.070	19	41	4.83 ± 0.97	16	34	1.89 ± 0.22	12	26	0.399 ± 0.056
24	48	0.927 ± 0.080	22	51	0.056 ± 0.003	19	42	1.99 ± 0.23	16	35	0.83 ± 0.11	12	27	0.120 ± 0.016
24	49	7.49 ± 0.60	22	52	0.004 ± 0.001	19	43	0.567 ± 0.059	16	36	0.239 ± 0.027	12	28	0.004 ± 0.001
24	50	30.0 ± 2.2	21	41	0.011 ± 0.001	19	44	0.088 ± 0.008	16	37	0.027 ± 0.003	11	23	0.280 ± 0.040
24	51	38.3 ± 2.4	21	42	0.421 ± 0.043	19	45	0.012 ± 0.001	16	38	0.005 ± 0.001	11	24	0.319 ± 0.041
24	52	33.8 ± 7.3	21	43	4.75 ± 0.49	18	35	0.019 ± 0.002	15	29	0.007 ± 0.001	11	25	0.078 ± 0.010
24	53	10.87 ± 0.50	21	44	12.1 ± 1.2	18	36	0.462 ± 0.053	15	30	0.081 ± 0.010	10	22	0.316 ± 0.053
24	54	2.85 ± 0.11	21	45	15.2 ± 1.6	18	37	2.03 ± 0.23	15	31	0.670 ± 0.080	10	23	0.041 ± 0.006
24	55	0.008 ± 0.001	21	46	8.1 ± 1.8	18	38	4.96 ± 0.55	15	32	1.22 ± 0.16			
23	45	0.028 ± 0.003	21	47	2.28 ± 0.20	18	39	2.69 ± 0.33	15	33	0.443 ± 0.058			

APPENDIX B

TABLE VII. Mean and rms values of longitudinal velocity of residual nuclei (cm/ns) in the iron beam system at rest at 1500*A* MeV (I = interpolated, see Sec. IIC).

Z	*A*	Mean velocity	rms	*Z*	*A*	Mean velocity	rms	*Z*	*A*	Mean velocity	rms
27	54	-0.079 ± 0.020	0.127	21	45	−0.106(I)	0.225	16	34	−0.186(I)	0.355
27	55	-0.058 ± 0.015	0.110	21	46	−0.104(I)	0.208	16	35	−0.180(I)	0.351
27	56	-0.033 ± 0.008	0.104	21	47	-0.098 ± 0.020	0.199	16	36	-0.183 ± 0.027	0.339
26	51	-0.093 ± 0.023	0.141	21	48	-0.089 ± 0.018	0.192	16	37	-0.176 ± 0.026	0.345
26	52	-0.056 ± 0.014	0.132	21	49	-0.080 ± 0.016	0.172	16	38	-0.165 ± 0.025	0.322
26	53	-0.035 ± 0.009	0.114	21	50	-0.082 ± 0.001	0.157	15	30	-0.213 ± 0.032	0.439
26	54	-0.031 ± 0.008	0.084	20	39	-0.160 ± 0.040	0.293	15	31	-0.201 ± 0.030	0.401
26	55	-0.034 ± 0.008	0.072	20	40	-0.131 ± 0.026	0.288	15	32	−0.198(I)	0.391
25	49	-0.089 ± 0.022	0.177	20	41	-0.129 ± 0.026	0.274	15	33	−0.197(I)	0.379
25	50	-0.078 ± 0.019	0.168	20	42	-0.130 ± 0.026	0.260	15	34	-0.196 ± 0.029	0.379
25	51	-0.052 ± 0.013	0.150	20	43	−0.132(I)	0.259	15	35	-0.187 ± 0.028	0.364
25	52	-0.053 ± 0.013	0.125	20	44	−0.135(I)	0.235	15	36	-0.162 ± 0.024	0.348
25	53	-0.061 ± 0.015	0.105	20	45	-0.116 ± 0.023	0.233	14	28	-0.221 ± 0.033	0.447
25	55	-0.032 ± 0.008	0.074	20	46	-0.105 ± 0.021	0.216	14	29	-0.218 ± 0.033	0.436
24	46	-0.112 ± 0.028	0.201	20	47	-0.102 ± 0.020	0.204	14	30	−0.219(I)	0.412
24	47	-0.104 ± 0.026	0.191	20	48	-0.097 ± 0.019	0.197	14	31	−0.210(I)	0.412
24	48	-0.084 ± 0.021	0.189	19	37	-0.167 ± 0.033	0.330	14	32	-0.202 ± 0.030	0.405
24	49	-0.069 ± 0.017	0.181	19	38	-0.145 ± 0.022	0.278	14	33	-0.202 ± 0.030	0.402
24	50	-0.070 ± 0.017	0.167	19	39	-0.144 ± 0.022	0.297	13	26	-0.242 ± 0.048	0.510
24	51	-0.056 ± 0.014	0.160	19	40	-0.145 ± 0.022	0.284	13	27	-0.232 ± 0.046	0.467
24	52	−0.529(I)	0.140	19	41	−0.137(I)	0.284	13	28	-0.221 ± 0.044	0.449
24	53	-0.045 ± 0.011	0.117	19	42	−0.135(I)	0.255	13	29	−0.220(I)	0.448
24	54	-0.023 ± 0.006	0.092	19	43	-0.121 ± 0.018	0.254	13	30	-0.206 ± 0.041	0.458
24	55	-0.040 ± 0.022	0.093	19	44	-0.119 ± 0.018	0.240	13	31	-0.182 ± 0.036	0.445
23	45	-0.118 ± 0.030	0.228	19	45	-0.112 ± 0.022	0.231	12	24	-0.225 ± 0.045	0.496
23	46	-0.095 ± 0.019	0.224	19	46	-0.122 ± 0.025	0.217	12	25	-0.207 ± 0.041	0.487
23	47	-0.084 ± 0.017	0.204	18	35	-0.157 ± 0.024	0.360	12	26	−0.20 (I)	0.485
23	48	-0.088 ± 0.018	0.183	18	36	-0.164 ± 0.025	0.342	12	27	-0.198 ± 0.040	0.465
23	49	−0.081(I)	0.168	18	37	−0.156±0.023	0.322	12	28	-0.218 ± 0.054	0.467
23	50	−0.074(I)	0.156	18	38	-0.158 ± 0.024	0.291	11	22	-0.223 ± 0.045	0.561
23	51	-0.064 ± 0.013	0.145	18	39	−0.148(I)	0.285	11	23	-0.220 ± 0.044	0.550
23	52	-0.060 ± 0.012	0.121	18	40	−0.132(I)	0.273	11	24	−0.218(I)	0.533
23	53	-0.061 ± 0.015	0.121	18	41	-0.136 ± 0.020	0.284	11	25	-0.214 ± 0.043	0.513
22	43	-0.123 ± 0.016	0.244	18	42	-0.128 ± 0.019	0.261	11	26	-0.216 ± 0.043	0.504
22	44	-0.107 ± 0.018	0.232	18	43	-0.128 ± 0.019	0.263	10	20	-0.266 ± 0.080	0.630
22	45	-0.097 ± 0.019	0.227	17	33	-0.136 ± 0.030	0.420	10	21	−0.260(I)	0.599
22	46	-0.103 ± 0.021	0.209	17	34	-0.177 ± 0.026	0.384	10	22	−0.250(I)	0.583
22	47	−0.098(I)	0.198	17	35	-0.169 ± 0.025	0.345	10	23	-0.237 ± 0.071	0.572
22	48	−0.089(I)	0.176	17	36	-0.158 ± 0.024	0.331	10	24	-0.153 ± 0.095	0.569
22	49	-0.086 ± 0.017	0.172	17	37	−0.156(I)	0.320	9	18	-0.253 ± 0.076	0.680
22	50	-0.074 ± 0.015	0.161	17	38	-0.153 ± 0.023	0.308	9	19	-0.260 ± 0.078	0.650
22	51	-0.075 ± 0.015	0.165	17	39	-0.151 ± 0.023	0.294	9	20	-0.260 ± 0.078	0.656
22	52	-0.056 ± 0.017	0.138	17	40	-0.146 ± 0.022	0.303	9	21	-0.225 ± 0.067	0.641
21	41	-0.136 ± 0.034	0.275	17	41	-0.125 ± 0.019	0.294	8	16	-0.240 ± 0.072	0.743
21	42	-0.123 ± 0.025	0.273	16	31	-0.163 ± 0.031	0.412	8	17	-0.230 ± 0.069	0.715
21	43	-0.113 ± 0.023	0.251	16	32	-0.194 ± 0.029	0.397	8	18	-0.250 ± 0.075	0.703
21	44	-0.118 ± 0.024	0.237	16	33	-0.183 ± 0.027	0.375				

TABLE VIII. Same as Table VII, but at 1000*A* MeV.

Z	*A*	Mean velocity	rms	*Z*	*A*	Mean velocity	rms	*Z*	*A*	Mean velocity	rms
26	51	-0.086 ± 0.022	0.144	21	47	-0.099 ± 0.020	0.191	16	38	-0.157 ± 0.024	0.311
26	52	-0.075 ± 0.019	0.117	21	48	-0.094 ± 0.019	0.181	15	28	-0.175 ± 0.044	0.000
26	53	-0.056 ± 0.014	0.099	21	49	-0.085 ± 0.017	0.168	15	29	-0.210 ± 0.031	0.415
26	54	-0.041 ± 0.010	0.066	21	50	-0.089 ± 0.022	0.152	15	30	-0.207 ± 0.031	0.410
26	55	-0.031 ± 0.008	0.056	20	38	-0.134 ± 0.034	0.148	15	31	-0.203 ± 0.030	0.392
25	48	-0.097 ± 0.024	0.182	20	39	-0.167 ± 0.033	0.293	15	32	-0.197(I)	0.371
25	49	-0.097 ± 0.024	0.178	20	40	-0.159 ± 0.032	0.272	15	33	-0.196(I)	0.359
25	50	-0.099 ± 0.025	0.158	20	41	-0.151 ± 0.030	0.262	15	34	-0.190 ± 0.028	0.352
25	51	-0.078 ± 0.019	0.138	20	42	-0.144 ± 0.029	0.000	15	35	-0.184 ± 0.028	0.342
25	52	-0.068 ± 0.017	0.118	20	43	-0.135(I)	0.245	14	27	-0.194 ± 0.049	0.475
25	53	-0.053 ± 0.013	0.098	20	44	-0.124(I)	0.229	14	28	-0.215 ± 0.032	0.432
25	55	-0.049 ± 0.015	0.068	20	45	-0.119 ± 0.024	0.218	14	29	-0.208 ± 0.031	0.418
24	46	-0.114 ± 0.028	0.205	20	46	-0.107 ± 0.021	0.204	14	30	-0.207 ± 0.031	0.405
24	47	-0.106 ± 0.027	0.199	20	47	-0.107 ± 0.021	0.193	14	31	-0.203 ± 0.030	0.390
24	48	-0.109 ± 0.027	0.178	20	48	-0.095 ± 0.019	0.168	14	32	-0.192 ± 0.029	0.382
24	49	-0.092 ± 0.023	0.166	19	36	-0.149 ± 0.030	0.000	14	33	-0.191 ± 0.029	0.361
24	50	-0.085 ± 0.021	0.143	19	37	-0.158 ± 0.032	0.311	13	24	-0.169 ± 0.042	0.624
24	51	-0.074 ± 0.019	0.130	19	38	-0.167 ± 0.033	0.305	13	25	-0.188 ± 0.038	0.517
24	52	-0.062(I)	0.112	19	39	-0.172 ± 0.034	0.282	13	26	-0.210 ± 0.042	0.494
24	53	-0.047 ± 0.012	0.104	19	40	-0.152 ± 0.030	0.275	13	27	-0.207 ± 0.041	0.456
24	54	-0.036 ± 0.009	0.085	19	41	-0.151(I)	0.268	13	28	-0.212(I)	0.441
23	44	-0.124 ± 0.031	0.000	19	42	-0.143(I)	0.256	13	29	-0.208(I)	0.423
23	45	-0.127 ± 0.025	0.235	19	43	-0.132 ± 0.020	0.243	13	30	-0.206 ± 0.041	0.427
23	46	-0.124 ± 0.025	0.208	19	44	-0.120 ± 0.018	0.232	13	31	-0.203(I)	0.393
23	47	-0.108 ± 0.022	0.193	19	45	-0.114 ± 0.017	0.213	12	22	-0.171 ± 0.051	0.569
23	48	-0.097 ± 0.019	0.174	18	35	-0.181 ± 0.036	0.340	12	23	-0.208 ± 0.052	0.000
23	49	-0.090 ± 0.018	0.158	18	36	-0.184 ± 0.028	0.317	12	24	-0.219 ± 0.044	0.521
23	50	-0.079(I)	0.150	18	37	-0.179 ± 0.027	0.311	12	25	-0.211 ± 0.042	0.496
23	51	-0.067 ± 0.013	0.133	18	38	-0.164 ± 0.025	0.290	12	26	-0.210(I)	0.466
23	52	-0.056 ± 0.011	0.122	18	39	-0.158(I)	0.282	12	27	-0.207(I)	0.451
23	53	-0.049 ± 0.010	0.110	18	40	-0.142 ± 0.021	0.266	12	28	-0.208 ± 0.042	0.455
23	54	-0.031 ± 0.009	0.102	18	41	-0.143 ± 0.022	0.262	11	21	-0.184 ± 0.055	0.611
22	43	-0.139 ± 0.028	0.240	18	42	-0.141 ± 0.021	0.256	11	22	-0.209 ± 0.042	0.598
22	44	-0.136 ± 0.027	0.227	18	43	-0.130 ± 0.020	0.250	11	23	-0.208 ± 0.042	0.547
22	45	-0.123 ± 0.025	0.216	17	33	-0.186 ± 0.037	0.362	11	24	-0.203 ± 0.041	0.511
22	46	-0.112 ± 0.022	0.195	17	34	-0.189 ± 0.028	0.352	11	25	-0.197 ± 0.039	0.503
22	47	-0.104(I)	0.195	17	35	-0.181 ± 0.027	0.334	11	26	-0.191 ± 0.038	0.493
22	48	-0.095(I)	0.176	17	36	-0.178 ± 0.027	0.311	10	19	-0.185 ± 0.055	0.652
22	49	-0.083 ± 0.017	0.162	17	37	-0.173(I)	0.303	10	20	-0.223 ± 0.067	0.627
22	50	-0.073 ± 0.015	0.146	17	38	-0.163 ± 0.024	0.294	10	21	-0.210(I)	0.607
22	51	-0.074 ± 0.015	0.145	17	39	-0.158 ± 0.024	0.293	10	22	-0.209(I)	0.556
22	52	-0.064 ± 0.013	0.126	17	40	-0.152 ± 0.023	0.278	10	23	-0.257 ± 0.077	0.545
21	40	-0.166 ± 0.033	0.274	16	31	-0.193 ± 0.039	0.397	9	18	-0.217 ± 0.065	0.687
21	41	-0.157 ± 0.031	0.268	16	32	-0.201 ± 0.030	0.372	9	19	-0.230(I)	0.639
21	42	-0.147 ± 0.029	0.259	16	33	-0.200 ± 0.030	0.360	9	20	-0.220(I)	0.624
21	43	-0.138 ± 0.028	0.239	16	34	-0.189(I)	0.335	9	21	-0.191 ± 0.057	0.647
21	44	-0.127 ± 0.025	0.221	16	35	-0.183(I)	0.334	8	17	-0.250(I)	0.692
21	45	-0.121(I)	0.221	16	36	-0.172 ± 0.026	0.316	8	18	-0.240(I)	0.680
21	46	-0.110(I)	0.203	16	37	-0.167 ± 0.025	0.314				

TABLE IX. Same as Table VII, but at 750*A* MeV.

Z	*A*	Mean velocity	rms	*Z*	*A*	Mean velocity	rms	*Z*	*A*	Mean velocity	rms
27	54	−0.060 ± 0.015	0.096	21	42	−0.136 ± 0.027	0.235	16	34	−0.202(I)	0.339
27	55	−0.058 ± 0.015	0.073	21	43	−0.143 ± 0.029	0.232	16	35	−0.195(I)	0.326
27	56	−0.049 ± 0.012	0.058	21	44	−0.153 ± 0.031	0.230	16	36	−0.202 ± 0.030	0.316
26	51	−0.083 ± 0.021	0.135	21	45	−0.145(I)	0.226	16	37	−0.190 ± 0.028	0.314
26	52	−0.053 ± 0.013	0.118	21	46	−0.131(I)	0.206	16	38	−0.173 ± 0.035	0.285
26	53	−0.050 ± 0.013	0.102	21	47	−0.123 ± 0.025	0.193	15	30	−0.153 ± 0.051	0.402
26	54	−0.043 ± 0.011	0.068	21	48	−0.109 ± 0.022	0.183	15	31	−0.211 ± 0.042	0.377
26	55	−0.036 ± 0.009	0.063	21	49	−0.105 ± 0.021	0.173	15	32	−0.210(I)	0.360
25	49	−0.093 ± 0.023	0.179	21	50	−0.106 ± 0.027	0.157	15	33	−0.202(I)	0.356
25	50	−0.087 ± 0.022	0.154	20	40	−0.162 ± 0.049	0.266	15	34	−0.227 ± 0.045	0.358
25	51	−0.075 ± 0.019	0.134	20	41	−0.159 ± 0.032	0.250	15	35	−0.187 ± 0.037	0.330
25	52	−0.076 ± 0.019	0.117	20	42	−0.167 ± 0.033	0.249	15	36	−0.201 ± 0.040	0.311
25	53	−0.063 ± 0.016	0.104	20	43	−0.158(I)	0.250	14	29	−0.212 ± 0.053	0.411
25	55	−0.022 ± 0.005	0.067	20	44	−0.150(I)	0.231	14	30	−0.223 ± 0.045	0.403
24	47	−0.107 ± 0.027	0.190	20	45	−0.145 ± 0.029	0.223	14	31	−0.220 ± 0.044	0.382
24	48	−0.093 ± 0.023	0.181	20	46	−0.128 ± 0.026	0.209	14	32	−0.219 ± 0.044	0.382
24	49	−0.094 ± 0.023	0.163	20	47	−0.121 ± 0.024	0.194	14	33	−0.195 ± 0.039	0.359
24	50	−0.094 ± 0.024	0.145	20	48	−0.122 ± 0.037	0.186	14	34	−0.198 ± 0.049	0.347
24	51	−0.089 ± 0.022	0.133	19	38	−0.199 ± 0.040	0.280	13	26	−0.240 ± 0.067	0.431
24	52	−0.072(I)	0.115	19	39	−0.189 ± 0.028	0.277	13	27	−0.223 ± 0.056	0.437
24	53	−0.053 ± 0.013	0.107	19	40	−0.184 ± 0.028	0.274	13	28	−0.228(I)	0.437
24	54	−0.041 ± 0.010	0.091	19	41	−0.179(I)	0.262	13	29	−0.224(I)	0.396
24	55	−0.030 ± 0.015	0.092	19	42	−0.164(I)	0.259	13	30	−0.246 ± 0.062	0.407
23	45	−0.136 ± 0.041	0.211	19	43	−0.158 ± 0.024	0.250	13	31	−0.228 ± 0.057	0.399
23	46	−0.117 ± 0.023	0.210	19	44	−0.148 ± 0.022	0.236	12	24	−0.140 ± 0.072	0.511
23	47	−0.111 ± 0.022	0.188	19	45	−0.136 ± 0.020	0.218	12	25	−0.226 ± 0.056	0.470
23	48	−0.117 ± 0.023	0.178	19	46	−0.142 ± 0.028	0.212	12	26	−0.230(I)	0.468
23	49	−0.109 ± 0.022	0.169	18	36	−0.156 ± 0.035	0.306	12	27	−0.259 ± 0.065	0.458
23	50	−0.086(I)	0.153	18	37	−0.178 ± 0.036	0.292	12	28	−0.214 ± 0.064	0.449
23	51	−0.073 ± 0.015	0.137	18	38	−0.184 ± 0.028	0.293	11	22	−0.123 ± 0.071	0.531
23	52	−0.072 ± 0.014	0.126	18	39	−0.169(I)	0.285	11	23	−0.238 ± 0.072	0.521
23	53	−0.060 ± 0.012	0.111	18	40	−0.181 ± 0.027	0.260	11	24	−0.220(I)	0.510
23	54	−0.119 ± 0.036	0.102	18	41	−0.179 ± 0.027	0.250	11	25	−0.253 ± 0.076	0.516
22	43	−0.130 ± 0.039	0.231	18	42	−0.161 ± 0.024	0.249	11	26	−0.209 ± 0.063	0.484
22	44	−0.123 ± 0.025	0.233	18	43	−0.162 ± 0.032	0.242	10	21	−0.246(I)	0.470
22	45	−0.127 ± 0.025	0.209	17	34	−0.152 ± 0.045	0.358	10	22	−0.240(I)	0.500
22	46	−0.133 ± 0.027	0.202	17	35	−0.215 ± 0.043	0.312	10	23	−0.299 ± 0.090	0.531
22	47	−0.122(I)	0.199	17	36	−0.201(I)	0.316	10	24	−0.193 ± 0.058	0.512
22	48	−0.106(I)	0.174	17	37	−0.190(I)	0.305	9	19	−0.293(I)	0.585
22	49	−0.101 ± 0.020	0.169	17	38	−0.183 ± 0.027	0.290	9	20	−0.280(I)	0.569
22	50	−0.084 ± 0.017	0.150	17	39	−0.172 ± 0.026	0.289	8	17	−0.300(I)	0.629
22	51	−0.089 ± 0.018	0.144	17	40	−0.167 ± 0.025	0.275	8	18	−0.310(I)	0.606
22	52	−0.083 ± 0.025	0.130	16	32	−0.188 ± 0.042	0.364				
21	41	−0.111 ± 0.033	0.245	16	33	−0.202 ± 0.040	0.348				

TABLE X. Same as Table VII, but at 500*A* MeV.

Z	*A*	Mean velocity	rms	*Z*	*A*	Mean velocity	rms	*Z*	*A*	Mean velocity	rms
27	53	-0.097 ± 0.013	0.106	21	46	−0.166(I)	0.203	17	38	-0.212 ± 0.032	0.287
27	54	-0.088 ± 0.012	0.090	21	47	-0.1880 ± 0.026	0.197	17	39	-0.205 ± 0.031	0.302
27	55	-0.073 ± 0.012	0.067	21	48	-0.120 ± 0.024	0.186	17	40	-0.127 ± 0.038	0.280
27	56	-0.074 ± 0.015	0.058	21	49	-0.088 ± 0.018	0.174	16	31	-0.286 ± 0.086	0.389
26	51	-0.076 ± 0.019	0.146	21	50	-0.095 ± 0.024	0.142	16	32	-0.240 ± 0.036	0.381
26	52	-0.066 ± 0.016	0.121	21	41	-0.195 ± 0.039	0.305	16	33	-0.236 ± 0.034	0.358
26	53	-0.049 ± 0.012	0.106	21	42	-0.188 ± 0.038	0.257	16	34	−0.231(I)	0.331
26	54	-0.034 ± 0.008	0.076	21	43	-0.176 ± 0.035	0.241	16	35	−0.228(I)	0.318
26	55	-0.027 ± 0.007	0.068	21	44	-0.162 ± 0.032	0.227	16	36	-0.223 ± 0.033	0.326
25	49	-0.122 ± 0.030	0.191	21	45	−0.179(I)	0.221	16	37	-0.209 ± 0.031	0.349
25	50	-0.103 ± 0.026	0.163	20	39	-0.220 ± 0.055	0.300	16	38	-0.128 ± 0.038	0.275
25	51	-0.081 ± 0.020	0.141	20	40	-0.192 ± 0.038	0.273	15	29	-0.257 ± 0.051	0.386
25	52	-0.066 ± 0.016	0.121	20	41	-0.186 ± 0.037	0.266	15	30	-0.234 ± 0.035	0.432
25	53	-0.057 ± 0.014	0.108	20	42	-0.182 ± 0.036	0.243	15	31	-0.232 ± 0.035	0.377
25	55	-0.024 ± 0.006	0.074	20	43	−0.175(I)	0.236	15	32	−0.224(I)	0.385
25	56	-0.160 ± 0.080	0.060	20	44	−0.160(I)	0.229	15	33	−0.220(I)	0.349
24	47	-0.137 ± 0.034	0.207	20	45	-0.149 ± 0.030	0.223	15	34	-0.218 ± 0.046	0.369
24	48	-0.124 ± 0.031	0.183	20	46	-0.134 ± 0.027	0.208	15	35	-0.262 ± 0.058	0.379
24	49	-0.109 ± 0.027	0.170	20	47	-0.104 ± 0.026	0.196	14	27	-0.303 ± 0.061	0.429
24	50	-0.090 ± 0.023	0.148	19	37	-0.225 ± 0.045	0.322	14	28	-0.266 ± 0.040	0.456
24	51	-0.092 ± 0.023	0.139	19	38	-0.216 ± 0.032	0.301	14	29	-0.251 ± 0.038	0.407
24	52	−0.068(I)	0.118	19	39	-0.199 ± 0.030	0.286	14	30	−0.246(I)	0.405
24	53	-0.049 ± 0.012	0.109	19	40	-0.193 ± 0.029	0.266	14	31	−0.238(I)	0.372
24	54	-0.041 ± 0.010	0.095	19	41	−0.183(I)	0.268	14	32	-0.225 ± 0.034	0.408
23	45	-0.171 ± 0.034	0.233	19	42	−0.175(I)	0.255	14	33	-0.213 ± 0.043	0.373
23	46	-0.150 ± 0.030	0.210	19	43	-0.165 ± 0.025	0.248	13	26	-0.258 ± 0.052	0.522
23	47	-0.131 ± 0.026	0.196	19	44	-0.156 ± 0.023	0.238	13	27	-0.234 ± 0.047	0.456
23	48	-0.119 ± 0.024	0.178	19	45	-0.120 ± 0.024	0.207	13	28	−0.230(I)	0.421
23	49	-0.117 ± 0.023	0.169	19	46	0.000 ± 0.000	0.000	13	29	−0.228(I)	0.407
23	50	−0.094(I)	0.152	18	35	-0.243 ± 0.049	0.342	13	30	-0.223 ± 0.045	0.472
23	51	-0.077 ± 0.015	0.140	18	36	-0.221 ± 0.033	0.320	12	24	-0.287 ± 0.057	0.550
23	52	-0.071 ± 0.014	0.129	18	37	-0.208 ± 0.031	0.313	12	25	-0.268 ± 0.054	0.475
23	53	-0.064 ± 0.013	0.118	18	38	-0.205 ± 0.031	0.295	12	26	−0.260(I)	0.425
22	43	-0.185 ± 0.037	0.258	18	39	−0.200(I)	0.283	12	27	−0.256(I)	0.447
22	44	-0.164 ± 0.033	0.230	18	40	−0.196(I)	0.251	12	28	-0.207 ± 0.041	0.482
22	45	-0.156 ± 0.031	0.218	18	41	-0.190 ± 0.028	0.274	11	22	-0.297 ± 0.074	0.593
22	46	-0.141 ± 0.028	0.201	18	42	-0.151 ± 0.023	0.253	11	23	-0.278 ± 0.080	0.570
22	47	−0.156(I)	0.193	18	43	-0.136 ± 0.027	0.218	11	24	−0.265(I)	0.573
22	48	−0.149(I)	0.174	17	33	-0.236 ± 0.047	0.381	10	22	−0.280(I)	0.528
22	49	-0.106 ± 0.021	0.169	17	34	-0.225 ± 0.034	0.362	10	23	-0.241 ± 0.100	0.597
22	50	-0.092 ± 0.018	0.153	17	35	-0.216 ± 0.032	0.334	10	24	-0.290 ± 0.102	0.577
22	51	-0.090 ± 0.018	0.149	17	36	−0.215(I)	0.323				
22	52	-0.081 ± 0.016	0.131	17	37	−0.213(I)	0.296				

TABLE XI. Same as Table VII, but at 300*A* MeV.

Z	*A*	Mean velocity	rms	*Z*	*A*	Mean velocity	rms	*Z*	*A*	Mean velocity	rms
27	54	-0.069 ± 0.015	0.084	22	48	−0.149(I)	0.172	17	35	-0.252 ± 0.038	0.335
27	55	-0.060 ± 0.012	0.065	22	49	-0.114 ± 0.035	0.164	17	36	−0.230(I)	0.292
27	56	-0.051 ± 0.011	0.058	22	50	-0.119 ± 0.030	0.157	17	37	−0.255(I)	0.295
26	51	-0.110 ± 0.023	0.136	22	51	-0.128 ± 0.030	0.147	17	38	-0.244 ± 0.037	0.283
26	52	-0.082 ± 0.021	0.115	21	42	-0.231 ± 0.046	0.248	17	39	-0.188 ± 0.043	0.274
26	53	-0.071 ± 0.018	0.106	21	43	-0.204 ± 0.041	0.237	17	40	-0.243 ± 0.036	0.265
26	54	-0.053 ± 0.013	0.094	21	44	-0.196 ± 0.039	0.226	16	32	-0.298 ± 0.060	0.367
26	55	-0.030 ± 0.007	0.073	21	45	−0.188(I)	0.211	16	33	-0.266 ± 0.040	0.344
25	49	-0.153 ± 0.038	0.162	21	46	−0.177(I)	0.201	16	34	−0.253(I)	0.333
25	50	-0.128 ± 0.032	0.150	21	47	-0.159 ± 0.032	0.186	16	35	−0.252(I)	0.322
25	51	-0.105 ± 0.026	0.135	21	48	-0.149 ± 0.030	0.186	16	36	-0.280 ± 0.065	0.320
25	52	-0.093 ± 0.023	0.130	21	49	-0.149 ± 0.034	0.172	16	37	-0.255 ± 0.038	0.306
25	53	-0.075 ± 0.019	0.107	20	40	-0.243 ± 0.049	0.264	16	38	-0.223 ± 0.045	0.288
25	55	-0.024 ± 0.006	0.072	20	41	-0.224 ± 0.045	0.257	15	30	-0.322 ± 0.064	0.398
24	47	-0.177 ± 0.044	0.182	20	42	-0.206 ± 0.041	0.247	15	31	-0.295 ± 0.044	0.375
24	48	-0.155 ± 0.039	0.177	20	43	−0.207(I)	0.238	15	32	−0.290(I)	0.370
24	49	-0.137 ± 0.034	0.162	20	44	−0.196(I)	0.221	15	33	−0.280(I)	0.348
24	50	-0.118 ± 0.029	0.154	20	45	-0.189 ± 0.038	0.215	15	34	-0.272 ± 0.041	0.344
24	51	-0.096 ± 0.024	0.139	20	46	-0.164 ± 0.033	0.202	15	35	-0.262 ± 0.039	0.321
24	52	−0.090(I)	0.131	20	47	-0.156 ± 0.031	0.195	14	28	-0.308 ± 0.062	0.413
24	53	-0.076 ± 0.019	0.103	19	38	-0.250 ± 0.050	0.285	14	29	-0.305 ± 0.046	0.389
24	54	-0.063 ± 0.016	0.101	19	39	-0.236 ± 0.035	0.282	14	30	−0.300(I)	0.378
23	46	-0.190 ± 0.038	0.201	19	40	-0.229 ± 0.034	0.269	14	31	−0.295(I)	0.319
23	47	-0.162 ± 0.032	0.188	19	41	−0.224(I)	0.261	14	32	-0.287 ± 0.064	0.392
23	48	-0.148 ± 0.030	0.180	19	42	−0.212(I)	0.243	13	26	-0.339 ± 0.102	0.447
23	49	-0.125 ± 0.025	0.170	19	43	-0.210 ± 0.031	0.242	13	27	−0.326(I)	0.400
23	50	−0.120(I)	0.155	19	44	-0.184 ± 0.037	0.217	13	28	−0.310(I)	0.336
23	51	-0.115 ± 0.023	0.138	19	45	-0.209 ± 0.042	0.201	13	29	-0.308 ± 0.082	0.365
23	52	-0.103 ± 0.021	0.135	18	36	-0.261 ± 0.039	0.314	12	25	-0.325 ± 0.098	0.385
23	53	-0.096 ± 0.019	0.124	18	37	-0.255 ± 0.038	0.297	12	26	−0.318(I)	0.394
23	54	−0.210(I)	0.250	18	38	-0.200 ± 0.042	0.278	12	27	-0.310 ± 0.098	0.395
22	43	-0.213 ± 0.043	0.210	18	39	−0.236(I)	0.279	12	28	-0.309 ± 0.093	0.407
22	44	-0.206 ± 0.041	0.224	18	40	-0.215 ± 0.032	0.264	11	23	-0.326 ± 0.098	0.384
22	45	-0.186 ± 0.037	0.209	18	41	-0.212 ± 0.032	0.272	11	24	−0.310(I)	0.365
22	46	-0.178 ± 0.036	0.195	18	42	-0.212 ± 0.042	0.238				
22	47	−0.135(I)	0.194	17	34	-0.272 ± 0.054	0.337				

[1] C. H. Tsao, R. Silberberg, A. F. Barghouty, L. Sihver, and T. Kanai, Phys. Rev. C **47**, 1257 (1993).
[2] R. Michel, M. Gloris *et al*., Nucl. Instrum. Methods B **103**, 183 (1995).
[3] W. R. Webber, J. C. Kish, J. M. Rockstroh, Y. Cassagnou, R. Legrain, A. Soutoul, O. Testard, and C. Tull, Astrophys. J. **508**, 949 (1998).
[4] W. R. Webber, J. C. Kish, J. M. Rockstroh, Y. Cassagnou, R. Legrain, A. Soutoul, O. Testard, and C. Tull, Astrophys. J. **508**, 940 (1998).
[5] W. R. Webber, J. C. Kish, and D. A. Schrier, Phys. Rev. C **41**, 533 (1990).
[6] W. R. Webber, J. C. Kish, and D. A. Schrier, Phys. Rev. C **41**, 547 (1990).
[7] W. R. Webber, J. C. Kish, and D. A. Schrier, Phys. Rev. C **41**, 520 (1990).
[8] G. D. Westfall, L. W. Wilson, P. J. Lindstrom, H. J. Crawford, D. E. Greiner, and H. H. Heckman, Phys. Rev. C **19**, 1309 (1979).
[9] C. Zeitlin, L. Heilbronn, J. Miller, S. E. Rademacher, T. Borak, T. R. Carter, K. A. Frankel, W. Schimmerling, and C. E. Stronach, Phys. Rev. C **56**, 388 (1997).
[10] E. C. Stone *et al*., Space Sci. Rev. **86**, 1 (1998).
[11] J. J. Connell, Space Sci. Rev. **99**, 41 (2001).
[12] HINDAS Final Report, EU Contract FIKW-CT-00031, edited by J. P. Meulders, A. Koning, and S. Leray (2005).
[13] S. Leray *et al*., Phys. Rev. C **65**, 044621 (2002).
[14] A. Letourneau *et al*., Nucl. Instrum. Methods B **170**, 299 (2000).
[15] C. M. Herbach *et al*., Nucl. Phys. **A765**, 426 (2006).
[16] F. Rejmund *et al*., Nucl. Phys. **A683**, 540 (2001).
[17] J. Benlliure *et al*., Nucl. Phys. **A683**, 513 (2001).
[18] W. Wlazlo *et al*., Phys. Rev. Lett. **84**, 5736 (2000).
[19] T. Enqvist *et al*., Nucl. Phys. **A686**, 481 (2001).
[20] B. Fernández-Domínguez *et al*., Nucl. Phys. **A747**, 227 (2005).
[21] L. Audouin *et al*., Nucl. Phys. **A768**, 1 (2006).
[22] J. Taïeb *et al*., Nucl. Phys. **A724**, 413 (2003).
[23] M. Bernas *et al*., Nucl. Phys. **A725**, 213 (2003).
[24] E. Casarejos *et al*., Phys. Rev. C **74**, 044612 (2006).
[25] J. Pereira *et al*., Phys. Rev. C **75**, 14602 (2007); J. Pereira, Ph.D. thesis, Universidad de Santiago de Compostela, Spain (2004).
[26] P. Chesny, A. Forgeas, J. M. Gheller, G. Guiller, P. Pariset, L. Tassan-Got, P. Armbruster, K.-H. Behr, J. Benlliure, K. Burkard, A. Brünle, T. Enqvist, F. Farget, and K.-H. Schmidt, GSI Annual Rep. 97-1, 1996, p. 190.
[27] B. Jurado, K.-H. Schmidt, and K.-H. Behr, Nucl. Instrum. Methods A **483**, 603 (2002).
[28] H. Geissel *et al*., Nucl. Instrum. Methods B **70**, 286 (1992).
[29] P. Napolitani, K. H. Schmidt, A. S. Botvina, F. Rejmund, L. Tassan-Got, and C. Villagrasa, Phys. Rev. C **70**, 054607 (2004).
[30] http://www-w2k.gsi.de/charms/secreac1.htm
[31] S. Kox *et al*., Phys. Lett. **B159** (1), 15 (1985).
[32] K.-H. Schmidt, J. Benlliure, and J. Pereira, Nucl. Instrum. Methods A **478**, 493 (2002).
[33] B. Mustapha, Ph.D. thesis, University of Paris XI, 1999, IPNO-T-99-05.
[34] R. Michel *et al*., Nucl. Instrum. Methods B **129**, 153 (1997).
[35] R. Michel *et al*., AIP Conf. Proc. **769**, 1551 (2005).
[36] W. R. Webber, J. C. Kish, and D. A. Schrier, Phys. Rev. C **41**, 566 (1990).
[37] K. Sümmerer and B. Blank, Phys. Rev. C **61**, 034607 (2000).
[38] R. Silberberg and C. H. Tsao, Phys. Rep. **6**, 351 (1990).
[39] R. Silberberg, C. H. Tsao, and A. F. Barghouty, Astrophys. J. **501**, 911 (1998).
[40] R. Silberberg and C. H. Tsao, Astrophys. J. Suppl. Ser. **25**, 315 (1973).
[41] G. Rudstam, P. C. Stevenson, and R. L. Folger, Phys. Rev. **87**, 358 (1952).
[42] H. W. Bertini, Phys. Rev. **131**, 1801 (1963).
[43] Y. Yariv and Z. Fraenkel, Phys. Rev. C **20**, 2227 (1979).
[44] A. Boudard, J. Cugnon, S. Leray, and C. Volant, Phys. Rev. C **66**, 044615 (2002).
[45] S. G. Mashnik and A. J. Sierk, in *Proceedings of the Fourth International Topical Meeting on Nuclear Applications of Accelerator Technology (AccApp00), Washington, DC, 2000* (American Nuclear Society, La Grange Park, IL, 2001), p. 328.
[46] R. E. Prael and H. Lichtenstein, User Guide to LCS: The LAHET Code System, LA-UR-89-3014, 1989 (unpublished).
[47] J. S. Hendricks *et al*., MCNPX 2.5d, report LA-UR-03-5916, 2003 (unpublished).
[48] L. Dresner, Oak Ridge Technical Rep. ORNL-TM-196 (unpublished).
[49] F. Atchison, in *Proceedings of Specialists' Meeting on Intermediate Energy Data, OECD, Issy-les-Moulineaux, France, May/June 1994*, p. 199 (unpublished).
[50] V. F. Weisskopf and D. H. Ewing, Phys. Rev. **57**, 472 (1940).
[51] A. R. Junghans *et al*., Nucl. Phys. **A629**, 635 (1998).
[52] S. Furihata, in *Proceedings of International Conference on Advanced Monte Carlo for Radiation Physics, Particle Transport Simulation and Applications* (Springer-Verlag, Berlin, 2000).
[53] R. J. Charity *et al*., Nucl. Phys. **A483**, 371 (1988).
[54] W. Hauser and H. Feshbach, Phys. Rev. **87**, 366 (1952).
[55] L. G. Moretto, Nucl. Phys. **A247**, 211 (1975).
[56] J. P. Bondorf *et al*., Phys. Rep. **257**, 133 (1995).
[57] R. P. Scharenberg *et al*., Phys. Rev. C **64**, 054602 (2001).
[58] E. Fermi, Prog. Theor. Phys. **5**, 570 (1950).
[59] B. C. Barashenkov, *Cross-Sections of Interactions of Particles and Nuclei with Nuclei* (JINR Publications, Dubna, 1993).
[60] A. Boudard *et al*., Nucl. Phys. **A663–664**, 1061c (2000).
[61] A. Botvina (private communication).
[62] K. K. Gudima, S. G. Mashnik, and V. D. Toneev, Nucl. Phys. **A401**, 329 (1983).
[63] S. R. Souza, W. P. Tan, R. Donangelo, C. K. Gelbke, W. G. Lynch, and M. B. Tsang, Phys. Rev. C **62**, 064607 (2000).
[64] D. J. Morrissey, Phys. Rev. C **39**, 460 (1989).
[65] S. G. Mashnik *et al*., AIP Conf. Proc. **769**, 1188 (2005).
[66] C. Villagrasa-Canton, Ph.D. thesis, University of Paris XI, 2003.